The interaction of calcium ions with specific residues in the SARS-CoV fusion peptide and the regulation of viral infectivity

Miya K. Bidon[1±], George Khelashvili[3±], Marco R. Straus[2], Tiffany Tang[1], Juliana Debrito Carten[1], Harel Weinstein[3*], Gary R. Whittaker[2*], and Susan Daniel[1*]

[1]Robert Frederick Smith School of Chemical and Biomolecular Engineering, Cornell University, Ithaca, NY, USA

[2]Department of Microbiology and Immunology, Cornell University, Ithaca, NY, USA

[3]Department of Physiology & Biophysics, Weill Cornell Medicine, New York, NY, USA

*Corresponding authors:

Susan Daniel: sd386@cornell.edu

Gary Whittaker: grw7@cornell.edu

Harel Weinstein: haw2002@med.cornell.edu

[±] These authors contributed equally.

Abstract

Viral envelope fusion with the host cell membrane is dependent on a specific viral fusion peptide (FP) or loop, which becomes exposed during virus entry to drive the process of membrane fusion. In coronaviruses, the FP is a highly conserved domain that sits in the center of spike protein and in SARS-CoV, is adjacent to the S2' proteolytic cleavage site. This peptide contains a hydrophobic LLF motif, as well as several conserved negatively charged amino acids that interact with Ca2+ ions to promote membrane fusion. In this work we perform a systematic mutagenesis study of the negatively charged amino acids within the SARS-CoV fusion peptide (FP1/FP2) and combine this with molecular dynamics simulations to define the membrane interactions that regulate virus infectivity. We show that the E801/D802 amino acid pair in the SARS-CoV FP is predicted to bind to one Ca^{2+} ion to promote FP-membrane interaction, with a second Ca^{2+} ion likely pairing residue D812 with either E821 or D825. The D812/D821 residue pair promotes membrane interaction, whereas the D821/D825 is inhibitory to membrane insertion. Taken together, our results demonstrate the dynamic nature of the coronavirus FP region that likely facilitates its interactions with and insertion into the host cell membrane.

Author Summary

Coronaviruses have reemerged as a highly pathogenic virus family through the rise of SARS-CoV, MERS-CoV, and more recently, SARS-CoV-2. As more transmissible variants of SARS-CoV-2 arise, it is imperative that we understand the mechanisms of CoV viral entry to enable the development of effective therapeutics. Recent reviews have suggested the repurposing of FDA-approved calcium channel blockers to treat infection by coronaviruses; however, calcium's method of

action on viral-host cell fusion events is unknown. We have found that increased calcium availability leads to increased viral infection across the CoV family, suggesting that calcium is involved in mediating the interaction between the viral fusion peptide and the host cell membrane. As such, we hypothesize that the highly conserved fusion peptide interacts directly with calcium and this interaction is required for viral entry and infection. Through mutagenesis studies of specific negatively charged residues in the fusion peptide, we have identified residues that impact viral infectivity. We have also compared the infectivity of wild-type and mutant CoV pseudoparticles in calcium-rich or -depleted environments using chelating drugs. Our data mirrors the residue coordination observed SARS-CoV-2, as both between SARS-CoV and SARS-CoV-2 FPs bind to two calcium ions. These results demonstrate the importance of Ca^{2+} for CoV FP function during viral entry and opens the possibility of utilizing FDA-approved calcium-blocking drugs as a treatment for COVID-19.

Introduction

Coronaviruses (CoVs) are a diverse family of enveloped, positive-sense, single-stranded RNA viruses responsible for causing respiratory and enteric diseases across a wide range of species [1, 2]. Three pathogenic human coronaviruses have emerged during the early 21st century: in 2002, severe acute respiratory syndrome (SARS-CoV) [3]; in 2012, Middle East respiratory syndrome (MERS-CoV) [4]; and presently, SARS-CoV-2 [5, 6]. The World Health Organization has listed coronaviruses as one of the top five emerging pathogens likely to cause major epidemics due to the minimal countermeasures that exist [7-9]. While vaccines are one strategy that has proven successful during this SARS-CoV-2 pandemic, there is an outstanding need for antiviral drugs as

a necessary parallel line of defense. To develop new antivirals, we need to understand the fundamental biology of the virus and its host interactions. From such knowledge we can therapeutically target well-conserved parts of the viral life cycle in order to confer the broadest protection. Viral entry is indeed a conserved function [10, 11], with the coronavirus spike (S) protein controlling virus entry through its interaction with the host cell plasma membrane. Examining the entry functions of the S protein can point to vulnerable targets that can be exploited for drug intervention.

The CoV S protein is composed of the S1 and S2 domains, which are responsible for facilitating receptor binding and membrane fusion, respectively [10, 12, 13]. CoVs utilize two different pathways to enter host cells: an “early” pathway, often referred to as the plasma membrane route, and a “late” pathway that follows the canonical endosomal pathway [10]. The pathway used by the virus is dependent on the host cell type, and more specifically, on the local protease environment [14]. The current thinking is that SARS-CoV, MERS-CoV and SARS-CoV-2 enter host cells via the early pathway when transmembrane-bound proteases (TTSPs), such as the TMPRSS2, are present. In cell lines lacking TTSPs, the virus enters cells via the endosomal route where it interacts with lysosomal proteases (*e.g.* cathepsin L) [10, 15, 16]. This pathway flexibility arises from the requirement for protease cleavage to prime the S protein for subsequent conformational changes needed to carry out membrane fusion. Two possible cleavage sites reside within the S protein: the S1/S2 site and the S2’ site [17]. The first site is located at the boundary of the S1 and S2 domains and is typically cleaved by furin during virus assembly. It is this cleavage by furin that separates the binding domain from the fusion machinery. The S2’ prime site is located next to the N-terminus of the conserved fusion peptide

(FP) segment that is liberated upon cleavage [18]. S2' cleavage allows the S2 domain to undergo a large conformational change that positions the FP for insertion into the host cell membrane [10]. FP membrane insertion is a key step in commencing the process of merging the host cell membrane with the viral envelope, resulting in the transfer of the viral genome into the host cell.

Given the importance of the FP in initiating membrane fusion, it is not surprising to find significant conservation of the amino acid sequence in this region of the S protein across many CoVs [19]. Due to its high degree of conservation, the FP stands out as a potential antiviral target. Thus, work carried out by our team and others has focused on understanding the structure and function of the FP. This work has identified conserved residues that interact with calcium ions (Ca^{2+}) and mediate the interactions between the host cell membrane and the FP that lead to viral infection [19-23].

In our previous studies, we showed that for both SARS-CoV and MERS-CoV, calcium depletion in cell culture leads to a significant drop in viral infection [19, 20]. We connected this decrease in infectivity to a defect in membrane fusion, observing that syncytia formation during cell-to-cell fusion between S- and ACE2 receptor-expressing VeroE6 cells also drops in calcium-depleted media. We then sought to connect this observed impact on membrane fusion with the molecular scale features of S that may interact directly with calcium ions. Within the S2 domain of S, the FP sequence contains highly conserved charged amino acids that flank the hydrophobic residues LLF, which interact with the host membrane upon FP insertion [19]. We posited that these charged residues function as sites for calcium ion binding that may stabilize the local structure of the FP and position it for optimal membrane insertion. Through a series of biophysical and biochemical techniques, our group confirmed that calcium interacts directly with the FP and that

this interaction can be linked to infectivity. Using isothermal calorimetry, we determined the stoichiometry of the interaction between the FP and calcium ions to be two calcium ions for SARS-CoV [19, 22] and one calcium ion for MERS-CoV [20]. From circular dichroism (CD) measurements, we observed that in the presence of calcium and membranes, the FP adopts a conformation with a higher degree of alpha helicity. From electron spin resonance spectroscopy (ESR) results we found lipid ordering increased upon FP insertion, which can create favorable conditions for membrane fusion; we also observed greater lipid ordering in the presence of Ca^{2+} [19, 24]. Recent findings show that calcium is necessary to promote viral entry across multiple coronaviruses, including SARS-CoV, MERS-CoV, and SARS-CoV-2 [22, 23]. Taken together, these results revealed that the FP requires calcium to adopt the proper structure needed for membrane insertion. Despite this initial model for the interaction of calcium with the negatively charged residues of the SARS-CoV FP [19], the field still lacks a detailed structural understanding of how Ca^{2+} ions stabilize the FP for membrane insertion.

Here, we present specific mechanistic insight gathered from mutagenesis studies and computational simulations of the SARS-CoV FP and calcium. This work predicts the preferred modes of calcium binding to the acidic residues of the SARS-CoV FP and how those modes likely regulate membrane interactions and subsequent infectivity. We first examined the effects of mutating individual and multiple charged residues in the SARS-CoV FP on cell fusion and viral infectivity in the presence or absence of calcium. This was done to identify FP charged residues that likely interact with calcium during viral entry. We then used corresponding molecular dynamics simulations of the system to interpret our mutagenesis results structurally. From these simulations we identified the structures and probabilities of the FP's modes of calcium binding in

1:1 and 2:1 stoichiometries, and predicted the structure of the SARS-CoV FP that is best suited for membrane penetration.

Results

Generation and characterization of the SARS-CoV wild-type and mutated fusion peptides

Various structural conformations of the SARS-CoV spike monomer have been solved using Cryo-EM [26]. From these structures, it is apparent that the fusion peptide contains an N-terminal alpha helix, with the hydrophobic LLF residues, and a C-terminal disordered loop known to participate in cysteine-mediated intramolecular disulfide bonding **(Fig 1A).** To begin to identify the SARS-CoV FP's modes of calcium binding, we performed charged-to-alanine substitutions of six highly conserved residues within the FP sequence (**Fig 1B**). We first made single amino acid (aa) substitutions (E801A, D802A, D812A, E821A, D825A, D830A) in the wild-type SARS-CoV FP, which was used as a control. The majority of the negatively charged residues that we mutated are highly conserved across SARS-CoV, MERS-CoV, and SARS-CoV-2 (**Fig 1C**).

The wild-type and mutant forms of the SARS-CoV S protein were then cloned into standard pcDNA3.1 expression vectors to facilitate their transient expression in HEK293T cells. Following confirmation of high transfection efficiency in our cells, S protein synthesis, trafficking to the cells' surface, and proteolytic cleavage were all assessed. To assay proteolytic cleavage of the WT and mutant S proteins, TPCK-trypsin was added to the cells' surface 24 hours after transfection and the S proteins were then isolated by cell-surface biotinylation. Biotinylated proteins were retrieved following cell lysis using streptavidin beads, resolved by gel electrophoresis and immunoblotted using a SARS-CoV S polyclonal antibody. The resulting

immunoblots displayed full length, uncleaved (S_0), and cleaved S2 subunit (S_2) SARS-CoV S species migrating at 180kDa and 80kDa, respectively (**Fig 2A**). SARS-CoV S mutants containing the single mutations D802A, D812A, E821A, D825A, and D830A have comparable steady-state levels of full-length protein in comparison to the wild-type protein, indicating that these mutations in the FP did not impair the synthesis or trafficking of S (**Fig 2A**). Additionally, proteolytic cleavage of the D802A, D812A, E821A, D825A, and D830A mutants occurred following treatment with TPCK-trypsin, indicating that these mutants were able to be primed for downstream fusion evens. We observed a higher molecular weight species running above the full-length S protein (**Fig 2**, (Higher order S)). We have determined that heating samples at 95°C with 5mM DTT for 10 minutes resolves this higher molecular weight band (data not shown), indicating that this species likely results from spike-based protein-protein interactions.

We were unable to detect steady-state levels of the E801A mutant on the spike immunoblots. To further probe the nature of this residue's importance, we substituted in the larger, nonpolar methionine (E801M), the polar and uncharged glutamine (E801Q), positively charged lysine (E801K) or negatively charged aspartic acid (E801D). None of these mutations, including the charge mimetic E801D, restored the steady-state levels of the S protein to that of wild-type, indicating the specific requirement of glutamic acid in this region of the FP (**Fig 2B**).

Analysis of the SARS-CoV FP single point mutations' effect on syncytia formation

To functionally test the ability of S protein mutants to induce cell-cell fusion, we performed a syncytia assay. To do this we transiently expressed the WT and mutated S proteins in VeroE6 cells, which are kidney epithelial cells that express the ACE2 receptor [26]. 24 hours

following transfection, we induced cell-cell fusion by treating the cells with trypsin to cleave the FP at the S2' site (R797). Syncytia formation was visualized by immunofluorescence using the fluorescently labeled SARS-CoV S antibody and DAPI stain to identify multinucleated S-expressing cells that had fused. Syncytia were quantified by counting every group of fused cells that had a minimum of 4 nuclei. As expected, VeroE6 cells expressing the WT S protein readily formed syncytia (**Fig 3A and B**). Conversely, cells expressing the D802A, D812A, E821A, D825A, and D830A mutants all exhibited very few syncytia, indicating a defect in cell-cell fusion (**Fig 3A and B; Fig S1)**.

Analysis of the SARS-CoV FP mutants' effect on viral infectivity

SARS-CoV is designated a Risk Group 3 Select Agent that requires a specialized biosafety level 3 (BSL-3) setting for experiments. Pseudoparticles can be used as safe surrogates of live SARS-CoV to enable experimentation in BSL-2 level conditions [27]. To generate SARS-CoV pseudoparticles in HEK293T cells, we used a three-plasmid co-transfection system, with plasmids encoding: (1) the full length CoV surface S protein, (2) the murine leukemia virus (MLV) core proteins *gag* and *pol*, or (3) a firefly luciferase reporter gene containing the MLV-MJ RNA packaging signal and flanked by long terminal repeat (LTR) sequences [27]. Upon successful particle fusion with a host cell membrane, the luciferase reporter RNA transcript is reverse transcribed, integrated into the cell genome and expressed, enabling a measurable readout of pseudoparticle entry. Our previous studies have shown that this approach works well for assessing the infectivity of MERS-CoV S [20], SARS-CoV S [19, 27], and SARS-CoV-2 S [28].

Incorporation of the WT and mutant S proteins into the SARS-CoV pseudoparticles was assessed using immunoblot analysis. Pseudoparticles with WT or the mutant S proteins D802A, D812A, E821A, D825A, and D830A show comparable levels of S protein incorporation (**Fig 4A**). As expected, we did not detect the E801A mutant in the SARS-CoV pseudoparticles, likely due to its low cellular expression or synthesis.

After confirming the incorporation of the wild-type and mutant spike proteins into the SARS-CoV pseudoparticles, we tested the infectivity of the pseudoparticles. As we have demonstrated previously, exposure of VeroE6 cells to WT SARS CoV pseudoparticles results in a robust luminescent signal 72 hours post infection, indicating successful viral entry **(Fig 4B)**. E821A- and D825A-containing pseudoparticles did not exhibit a significant change in infectivity compared to wild-type particles, suggesting these individual residues do not have a major effect on FP function when calcium is present (**Fig 4B**). In contrast, the D802A, D812A, and D830A mutant pseudoparticles all showed a pronounced decrease in infectivity, with the D812A and D830A mutations resulting in essentially noninfectious particles. These results indicate that mutations in these three highly conserved negatively charged residues in the S protein's FP significantly decrease SARS-CoV pseudoparticle infectivity in calcium-containing conditions.

We next tested the effect of depleting extracellular calcium on the pseudoparticles' ability to infect VeroE6 cells using the chelator ethylene glycol-bis (ß-aminoethyl ether)-*N,N,N'N'*-tetraacetic acid (EGTA). We have previously studied the effects of calcium on viral infectivity and adopted similar calcium depletion methods in this study [19, 20]. Briefly, we treated VeroE6 cells with 50 µM EGTA prior to and during infection. Following incubation with the chelating agent, VeroE6 cells were inoculated with WT or mutant S protein-containing pseudoparticles and

incubated for 72 hours. Cells were then lysed and luminescence was quantified as a measure of pseudoparticle infectivity (**Fig 4B**). In support of our previous work [19], depletion of extracellular calcium had a marked effect on WT pseudoparticle infectivity, decreasing it to approximately half that of cells infected with WT pseudoparticles in the absence of EGTA (**Fig 4B**). Cells exposed to pseudoparticles containing either D802A or the D825A mutations also exhibited a further drop in infectivity, with the D825A mutation having the greatest additional reduction in infectivity (**Fig 4B**). The depletion of extracellular calcium had an additive effect on the decrease in infectivity in the context of specific FP mutations (D802A, D825A). These results suggest that these negatively charged residues in the FP are affected either directly or indirectly by loss of extracellular calcium.

We then examined the effect of intracellular calcium depletion on pseudoparticle infectivity by using the cell-permeable calcium chelator 1,2-bis(2-aminophenoxy)ethane- *N,N,N'N'*-tetraacetic acid tetrakis (BAPTA-AM). We have previously optimized the concentrations of BAPTA-AM so as not to significantly impact cell viability [19, 20]. VeroE6 cells were treated with 50 µM BAPTA-AM briefly prior to and during pseudoparticle infection, then harvested and assayed for luminescence (**Fig 4C**). Interestingly, depletion of intracellular calcium rendered the WT pseudoparticles noninfectious; similar results were observed across the WT and all mutant pseudoparticles tested; none of the pseudoparticles were infectious. In general, these data suggest that depletion of intracellular calcium exerts a more severe effect on pseudoparticle infectivity and point to the endosomal pathway as the primary route of pseudoparticle entry.

From our infectivity data we deduced that the FP likely uses multiple negatively charged residues to bind to multiple calcium ions. This is supported by the further decrease in infectivity of Spike E802A- and D825A-containing pseudoparticles when extracellular calcium is depleted.

We hypothesize that mutating those residues individually does not lead to a complete loss in pseudoparticle infectivity, since other charged residues in the FP can compensate by binding calcium; however, removal of calcium from the medium mimics the loss of those additional residues, leading to the FP's inability to bind calcium and a loss in infectivity.

Multiple negatively charged residues mediate SARS-CoV fusion peptide's calcium binding

To test the hypothesis that the FP utilizes alternative residues to mediate calcium binding, we created pairwise and triple residue substitutions within the S protein's FP. The FP contains two defined regions: the N-terminal region starting just upstream from the S2' cleavage site (aa798-819), termed FP1, and the downstream region that includes a critical disulfide bond (aa820-837), termed FP2 [18, 29]. Lai *et al.* has reported a stoichiometry of two calcium ions per single SARS-CoV FP, therefore we predict that FP1 and FP2 regions each contain residues that can coordinate calcium binding [19]. In FP1, the alanine substitutions of residues D802, and D812 rendered their pseudoparticles non-infectious; in FP2, the D825A and D830A substitution also led to non-infectious pseudoparticles. To investigate if individual substitutions of these three residues changed the mode of calcium binding, we created a complete set of their double mutants (E821A/D825A, E821A/D830A, D825A/D830A), and a triple mutant (E821A/D825A/D830A) (**Fig 5A**).

We first confirmed that these mutants were synthesized, trafficked to the plasma membrane, and were able to be cleaved by trypsin, as we had done with the single mutants (**Fig 5B**). We also tested the functionality of these S mutants using the previously described syncytia assay. VeroE6 cells transiently expressing either a double mutant (E821A/D825A, E821A/D830A,

D825A/D830A) or the triple mutant (E821A/D825A/D830A) all displayed fewer syncytia compared to WT S-expressing cells (**Fig 5C and D)**.

We then generated pseudoparticles containing the double and triple mutants and assayed the incorporation of the various mutants into the particles by immunoblotting for the spike protein. The double mutant E821/D830A- and D825A/D830A-containing pseudoparticles incorporated roughly equal amounts the S protein, while the triple mutant pseudoparticles (E821A/D825A/D830A) showed slightly reduced protein levels (**Fig 5E**). The E821A/D825A mutant particles exhibited significantly decreased protein levels indicating that although this mutant could be expressed and trafficked to the plasma membrane, its incorporation into pseudoparticles was diminished. We acknowledge the general low protein levels of the double and triple S mutants in our pseudoparticles as being a potential confounding variable. Nevertheless, we infected VeroE6 cells with the WT and mutant S protein pseudoparticles to investigate if multiple mutations in negatively charged residues of the FP caused a more pronounced decrease in infectivity. As was previously demonstrated, WT pseudoparticles are able to infect VeroE6 cells, with subsequent depletion of extra- or intra-cellular calcium causing a partial and then complete loss of infectivity, respectively **(Fig 5F and G).** Infectivity was dramatically reduced for all mutants in comparison to WT pseudoparticles, irrespective of extra- and intracellular calcium depletion. (**Fig 5F and G**). These data support the hypothesis that the SARS-CoV FP contains multiple sites of calcium binding, which when mutated result in a nonfunctional spike protein irrespective of calcium levels.

Molecular Dynamics simulations identify the modes of the SARS-CoV FP's Ca^{2+} binding

The effects that the various S mutants have on SARS CoV pseudoparticle infectivity suggests that the FP contains multiple sites of Ca^{2+} binding that are required for viral entry. This confirmed requirement of $Ca^{2+}$for FP function prompted an analysis of the predicted modes of Ca^{2+} binding in the wild-type and mutant SARS-CoV FPs. To this end, we carried out extensive atomistic molecular dynamics (MD) simulations of all the SARS-CoV FP constructs studied here (see Methods section). To monitor the spontaneous binding of Ca^{2+} to the FP, we collected 18 independent MD trajectories of 640ns in length for each construct. Following the analysis protocols described recently for SARS-CoV-2 FP simulations [23], the various modes of interactions between the SARS-CoV FP and Ca^{2+} ions were assessed in the trajectories by monitoring: i) the distances between the Ca^{2+} ions in solution and the side chains of all acidic residues in the peptide; and ii) the pairwise distances between the side chains of all acidic residues. Summarized in **Fig S2** are the observed events of simultaneous association of two Ca^{2+} ions with various pairs of FP residues in the individual trajectories of the WT and the mutant systems (see *red* and *blue* rectangles). The combined statistics for each construct (*i.e.,* the total number of binding events for different pairs of residues) are summarized in **Fig 6**.

These results show the modes of Ca^{2+} coordination in the WT protein, identifying the most frequent modes involving residue pairs E821/D825 (5 out of 18); E801/D802 and E801/D830 (4/18 each); and D812/E821 (2/18). Notably, a similar pattern of coordination preference was observed in our recent computational studies of Ca^{2+} association with SARS-CoV-2 FP [23]. Moreover, simultaneous binding of Ca^{2+} ions to the SARS-CoV-2 FP residue pairs equivalent to E801/D802 and D812/E821 produced the peptide conformations prone to membrane

302 penetration. In contrast, conformations that stabilized Ca^{2+} binding to residues equivalent to the
303 E821/D825 pair did not enable sustained bilayer insertion.

304 From these MD simulations of the SARS-CoV FP constructs, we were able to predict the
305 phenotypes for each construct (active or inactive). The mode of Ca^{2+} ion association predicted to
306 be inhibitory for membrane insertion (E821-D825) is shown in *red*, and the modes of Ca^{2+}
307 association predicted to facilitate membrane insertion are depicted in *green* boxes (**Fig 6**). In
308 those constructs with single mutations that were predicted to not have fusion activity (i.e.,
309 E801A, D802A, D812A, and D830A) we showed that only the Ca^{2+}-coordination mode involving
310 the E821/D825 pair persists, but not the D812/E821 pair of residues (**Fig 6**). Conversely, in the
311 SARS-CoV FP single mutants that maintained WT-like fusion activity (E821A and D825A), we did
312 not observe the E821/D825 residues predicted to participate in calcium binding. In these
313 function-preserving mutants we identified additional modes of Ca^{2+} binding that are enhanced in
314 comparison to the WT system: E801/D802 in mutant E821A, or E801/D830 in mutant D825A. For
315 the SARS-CoV FP constructs with multiple mutations, our MD trajectories revealed an overall
316 reduced Ca^{2+} binding ability (**Fig 6** and **Fig S3**), consistent with our experimental findings that (i)
317 these constructs are severely defective in the cell-cell fusion (**Fig 5C and D**) and infectivity assays,
318 and (ii) their function does not depend on the levels of either extracellular or intracellular Ca^{2+}
319 (**Fig 5F and G**).
320
321 **SARS-CoV FP propensity for membrane insertion is regulated by modes of Ca^{2+} binding.**
322 Overall, the above computational results reveal that the Ca^{2+} binding patterns of SARS-
323 CoV FP are very similar to those of SARS-CoV-2 FP. On this basis, membrane insertion of the SARS-

CoV FP could be expected to be enhanced by the modes of Ca^{2+} binding involving the E801/D802 and D812/E821 pairs of residues, and to be reduced by the ones involving the E821/D825 pair. To test this premise, we carried out MD simulations of two models of the WT SARS-CoV FP spontaneously associating with the lipid membrane (see **Methods**). In one, the peptide was interacting with 2 Ca^{2+} ions at the E801/D802 and D812/E821 sites (Model 1), and in the second, 2 Ca^{2+} ions were bound to the E801/D802 and E821/D825 pairs (Model 2). Each structure was simulated in 36 independent replicates, each run for ~0.9-1.0μs (see **Methods**).

Analysis of these trajectories revealed that, indeed, Model 1 extensively penetrated the membrane, while the membrane insertion of the Model 2 was negligible. This can be seen from the plots presented in **Fig 7** comparing frequencies of membrane insertion for each SARS-CoV FP residue in the simulations of Model 1 and Model 2 structures. The membrane insertion was quantified by monitoring the z-coordinate of the C_α atom of each residue in the peptide. A residue was inserted into the membrane if the z-distance between its C_α atom and the second carbon atom in the tail of a POPC lipid (atom C22 in CHARMM36 notation) was <5Å. As shown in **Fig 7A**, in Model 1, the N-terminal FP1 segment of the fusion peptide shows strong propensity for bilayer insertion, while in Model 2 the insertion is minimal (**Fig 7B**).

The detailed analysis of the individual trajectories in the Model 1 set revealed two distinct modes of bilayer penetration for SARS-CoV FP, similar to our findings for the SARS-CoV-2 FP. Thus, the Model 1 construct penetrates the bilayer either with its N-terminal LLF motif (**Fig 7C**) or with the more centrally located hydrophobic F815-M816 segment (**Fig 7D**). Interestingly, the two insertion modes appear to alternate which Ca^{2+} ion is neighboring the inserted portion. Thus, when the LLF is inserted, the Ca^{2+} ion associated with the neighboring E801/D802 residues is

bound to the membrane while the other Ca^{2+} binding site (D812/E821) is situated away from the membrane surface (see snapshot in **Fig 7C**). In case of the F815-M816 insertion, the position of the Ca^{2+} binding loci with respect to the membrane is reversed – the one associated with the D812/E821 pair is membrane-bound, while the E801/D802 pair is located farther from the bilayer (snapshot in **Fig 7D**). We also note that in both cases, the remaining anionic residues in the peptide (*i.e.* the ones not engaged with the Ca^{2+} ions) are either solvent exposed (D830) or engaged with electro-neutralizing interactions with neighboring basic residues (D825/R829, **Fig 7C and D**). These results support a mechanistic model in which membrane penetration of the SARS-CoV FP is significant only for specific modes of Ca^{2+} binding to the peptide, i.e., to the E801/D802 and D812/E821 pairs of conserved acidic residues. Moreover, Ca^{2+} binding at the E821/D825 pair is predicted to inhibit membrane insertion.

Discussion

The resurgence of pathogenic human coronaviruses brings about an immediate need for improving countermeasures to combat these global health threats. Increasing our knowledge of the mechanisms of viral entry is essential to develop broad-spectrum vaccines and antivirals. Viral entry is a critical step in the viral life cycle that is mediated by the S viral protein [8, 30, 31]. The S protein's FP is responsible for mediating viral and host cell membrane fusion. This region is highly conserved across the *Coronaviridae* viral family and understanding it how it functions may lead to the development of more broad-acting therapeutics. Previous work has highlighted the role that cations play in viral fusion, specifically Ca^{2+}. The electrostatic interactions between cations and negatively charged residues in the fusion peptide promote membrane fusion, leading

368 to higher infectivity [19-22, 32]. Lai et al. has proposed that two Ca^{2+} ions were needed to interact
369 with SARS-CoV FP; in each of the subdomains (FP1 and FP2), one Ca^{2+} coordinates two negatively
370 charged residues to allow the FP to adopt a conformation that promotes membrane insertion
371 [19].

372 To interrogate the requirement of the negatively charged residues in the SARS CoV fusion
373 peptide for its function, we first made single charge-to alanine substitutions in those residues
374 (**Fig 1**). Following transient expression of these mutants in Vero6 cells, we confirmed that
375 mutants D802A, D812A, E821A, D825A, and D830A were synthesized, accumulated to levels
376 comparable to the WT protein, and were trafficked to the plasma membrane (**Fig 2**). We further
377 confirmed the cell surface localization of these same FP mutants by treating VeroE6 cells
378 expressing these mutants with trypsin to assess their cleavage, after which we retrieved the FPs
379 using a cell surface biotinylation assay (**Fig 2**). The majority of the FP mutants assayed exhibited
380 cleavage following treatment with trypsin, indicating the accessibility of the S1/S2 cleavage site.
381 The E801A mutant was not detected on our spike immunoblots and further attempts to
382 understand this occurrence through additional substitutions did not result in the detection of this
383 mutant. We hypothesize that the absence of glutamate at position 801 in the fusion peptide
384 causes a loss in protein stability, though further work is needed to determine the significance of
385 this residue in the fusion peptide.

386 We next tested the fusion competency of the single FP mutants we had created using a
387 syncytia assay, which utilizes fusion events in cells transiently expressing the FP as a readout of
388 FP fusion activity. All of the single FP charged-to-alanine mutants the were detected on the spike
389 immunoblot (E801A, D802A, D812A, E821A, D825A, and D830A) exhibited a pronounced fusion

defect, as evidenced by the low number of fused VeroE6 cells, or syncytia, that were observed (**Fig 3**). Taken together, these data suggest that the highly conserved, negatively-charged residues within the FP individually contribute in a non-redundant manner to the function of the fusion peptide. However, due to the limitations and variability of the syncytia assay, we chose to use SARS-CoV2 pseudoparticles to mimic a more in vivo-like system to examine the functionality of the various FP mutants. Successful pseudoparticle entry into host cells results in the integration of the luciferase reporter gene into the cellular genome. Luminescence can therefore be used as a readout of pseudoparticle infectivity. We first confirmed the incorporation of the WT and single-charged-to-alanine mutant FPs into the pseudoparticles (**Fig 4A).** Nearly all FP mutants generated (E801A, D802A, D812A, E821A, D825A, and D830A) were incorporated in the SARS-CoV2 pseudoparticles; the E801A mutant was not detected.

We then infected VeroE6 cells using the SARS-CoV2 pseudoparticles we had generated and measured luminescence as a readout of infectivity and a proxy for viral entry. Introduction of WT pseudoparticles into VeroE6 cells results in a robust luminescence signal, indicating successful viral entry and fusion competency of the viral particles when calcium levels are unperturbed (**Fig 4B and C**). Infections with E821A and D825A-containing pseudoparticles at physiological levels of calcium also resulted in luminescence levels comparable to WT-containing pseudoparticles, suggesting that these residues are not required for FP function. To the contrary, pseudoparticles containing the D802A, D812A, or D830A mutations were unable to infect VeroE6 cells, resulting in aa significant drop in luminescence. These data indicate that when intra- and extra-cellular calcium levels remain unchanged, loss of an individual negative charges at positions

411 D802, D812, or D830 is sufficient to cause a substantial decrease in infectivity, likely due to a
412 defect in FP-mediated viral fusion and subsequent viral entry.

413 We then proceeded to test the requirement of extracellular calcium on the infectivity of
414 our FP-containing pseudoparticles by treating the cells with EGTA, a calcium-preferring chelator,
415 prior to infection. Removal of extracellular calcium resulted in a significant drop in the infectivity
416 of WT FP-containing particles, which is consistent with the known requirement of calcium for
417 SARS CoV2 viral entry (**Fig 4B**). Interestingly, pseudoparticles containing either the D802A or
418 D825A mutant showed a further reduction in infectivity when the extracellular calcium was
419 depleted. This suggests that multiple negatively charged residues in the FP are involved in calcium
420 binding and while loss of a single negative charge may not be sufficient to completely disrupt
421 infectivity, multiple "hits" are. Thus, removal of extracellular calcium mimics the loss of additional
422 electrostatic interactions needed for FP function, resulting in a further decrease in infectivity.
423 Pseudoparticles containing either the D812A or D830A FP mutant were essentially non-infectious
424 in the presence or absence of extracellular calcium. These results implicate residues D812A and
425 D830A in FP function; however, their specific roles as they relate to calcium cannot be teased
426 apart in this system.

427 We also depleted intracellular calcium levels using the cell permeable calcium chelator
428 BAPTA-AM, in order to test the contribution of intracellular (endosomal) during pseudoparticle
429 infectivity.

430

431 Following treatment with BAPTA-AM, WT FP-containing pseudoparticles are no longer
432 infectious (**Fig 4C**), indicating that intracellular calcium, specifically in the endosome, contributes

433 to pseudoparticle entry (**Fig 4B and C**). We propose that chelation with EGTA likely removed
434 the majority of extracellular calcium causing a 50% reduction in infectivity of WT FP-containing
435 pseudoparticles; however, it is known that SARS-CoV enters cells via two pathways: the plasma
436 membrane and endosomal pathways. Hence, the partial reduction in viral infectivity in the
437 presence of EGTA and then the complete loss of infectivity in the presence of BAPTA-AM may
438 reflect the SARS-CoV pseudoparticles' usage of these two pathways as well. It is important for
439 us to acknowledge that we cannot rule out the potential impact that depletion of intracellular
440 calcium may have on the integration, expression, or synthesis of the reporter transgene in the
441 pseudoparticle. However, we performed cell viability assays to optimize the concentrations of
442 both chelators used in this study and are confident that treatments with EGTA and BAPTA-AM
443 did not induce toxicity in the VeroE6 cells.

444 Given that the results from our infectivity assay suggested the involvement of multiple
445 calcium-binding residues in the fusion peptide, we then generated double mutants (E821A,
446 E825A; E821A, D830A; E825A, D830A) and a triple mutant (E821A:E825A;D830A) of the FP (**Fig**
447 **6A**). We validated the expression, synthesis, and cell surface localization of these mutants, as
448 well as their ability to be cleaved by trypsin (**Fig 6B**). As with the single mutants, we observed a
449 fusion defect in VeroE6 cells transiently expressing these mutant constructs, evidenced by the
450 few number of syncytia formed in comparison to cells expressing the WT FP (**Fig 6D**). When then
451 assayed the fusion activity of these mutants using the previously described pseudoparticle
452 infectivity assay. The double mutants E821A; D830A and E825A; D830A and a triple mutant
453 E821A; E825A; D830A were all incorporated into the pseudoparticles; the E821A; E825A mutant
454 was not (**Fig 6C**). If the FP binds calcium using more than one negatively charged residue, then

pseudoparticles containing the double or triple charge-to alanine mutants should exhibit a further decrease in infectivity. In comparison to WT FP-containing pseudoparticles, the FP double mutants E821A; D830A and E825A; D830A and the triple mutant E821A;E825A;D830A we assayed showed a complete loss in infectivity. Because the FP double mutant E821A, E825A was not incorporated into the pseudoparticles, we could not fully assess the impact of these mutations on FP function; however, the low number of syncytia observed in cells expressing this mutant suggests these residues are important for FP function. In summary, these results support the hypothesis that the SARS-CoV2 fusion peptide requires multiple negatively charged residues to bind to calcium during viral entry. Specifically, our data implicate FP residues D802 and D825 in coordinating the FP's interaction with calcium.

To better understand how the various charged residues in the SARS-CoV FP coordinate calcium binding, we undertook molecular dynamic (MD) simulations with the FP and calcium ions. The MD simulations of the Ca^{2+}-loaded peptide with the membrane illuminated the way Ca^{2+} binding to FP binding may affect its function. Exploring the probability of each FP residue interacting with the membrane in the identified Ca^{2+}-binding modes reveals the preferred mode of peptide insertion to be with the N-terminal end interacting with a calcium ion coordinated by residues E801 and D802 (**Fig 7**). The depth of insertion and the determinant role of the Ca^{2+} ion in facilitating membrane insertion are identical to the findings for the SARS-CoV-2 peptide and are in agreement with the experimental measurements of SARS-CoV FP membrane insertion by Lai *et al* [19, 20, 22]. That Ca^{2+} interacts with the same highly conserved, charged residues in the FPs of SARS-CoV and SARS-CoV-2 is not surprising.

476 Results from our computational modeling of SARS-CoV FP-membrane interactions in the
477 presence of Ca^{2+} show that the propensity of the SARS-CoV FP for membrane insertion is dictated
478 by specific modes of Ca^{2+} binding. The Ca^{2+} binding mode that enables the most sustained
479 membrane penetration involves the initial association of the peptide with the bilayer through a
480 Ca^{2+} binding site located near the N-terminus of the peptide. This site (E801/D802) is made
481 accessible following enzymatic cleavage and is inserted into the membrane via the insertion of
482 the juxtaposed hydrophobic segment (the LLF motif). In this process, all anionic residues of the
483 peptide are either engaged with Ca^{2+} ions, with neighboring basic residues, or remain solvent
484 exposed away from the membrane. Based on the preferred modes of Ca^{2+}-loaded FP interaction
485 with the membrane, we propose that the binding of Ca^{2+} following S protein cleavage at the S2'
486 site creates an energetically feasible membrane insertion process (**Fig 7A**) composed of the
487 following steps: (1) steering of the peptide towards the bilayer surface; (2) exposure of the
488 hydrophobic layer of the membrane to the conserved N-terminal LLF motif of the FP anchored
489 by the Ca^{2+} interactions with the phospholipid headgroups; and (3) shielding of the anionic
490 residues of the peptide by the preferred inserting conformation of the FP to prevent their
491 negative charge from interfering with membrane insertion. These three components became
492 evident from the analysis of the MD simulation trajectories presented here for the SARS-CoV FP
493 and bear a very high similarity to results from computational studies of the SARS-CoV-2 FP
494 (PMID: 33631204).

495 Remarkably, in both the SARS-CoV-2 FP simulations [23] and here, we observed a Ca^{2+} binding
496 mode that inhibits long-lasting membrane insertion. In this mode Ca^{2+} association with the
497 E821/D825 pair (corresponding to the D839/D843 in SARS-CoV-2 FP) positions the LLF motif near

the negatively charged D812 residue at the membrane surface (**Fig 7B**). This eliminates the favorable effect of the negative charge screening by the Ca^{2+}, so that the peptide bilayer encounters are transient and do not lead to penetration by the LLF motif. This mechanistic model, which highlights the role of the positioning of D812 residue in specific Ca^{2+} binding modes, is supported by our findings for the SARS-CoV S mutants, as it was previously found to be an impactful mutation in the SARS-CoV FP [18]. A recent study from Koppisetti *et al* asserts that a Ca^{2+} may be binding to D843/D849 in SARS-CoV-2 FP (corresponding to D825/D830 in SARS-CoV FP); however, as shown from the simulations in this study and Khelashvili *et al*, there is a high likelihood that second Ca^{2+} ion will bind to D812/D821 (corresponding to the D830/D839 in SARS-CoV-2 FP) for the maximal membrane penetration [23, 25]. Recent NMR studies regarding the membrane interaction with the fusion peptide still have yet to be fully resolved as current models use bicelles [25] and micelles [33], which do not completely capture the composition of the bilayer as was done for the computational modeling shown here; though the model of membrane insertion proposed by Koppisetti *et al* [25] most aligns with our proposed CoV FP interaction with bilayer (**Fig 8**). Thus, as shown in **Figs 6 and 7**, mutations that creates a high propensity for the Ca^{2+} binding mode involving the E821/D825 pair, stabilize peptide conformations that are non-productive for membrane penetration and are found here to inactivate the FP (**Fig 6**).

Interestingly, though our computational studies did not confirm the role of D830 with Ca^{2+}, our biological studies still reaffirmed its importance in the FP. Current studies on SARS-CoV-2 S protein classified the disordered portion of the FP in the FP2 domain as the FPPR (fusion peptide proximal region), which includes the charged residues D839/D843/D848 or E821/D825/D830 equivalent in SARS-CoV FP [23, 34]. This FPPR region was determined to be important, as it binds

to the RBD through the CTD1, and maintains the closed pre-fusion S trimer [34]. This is due to the tight packing around the disulfide bond reinforced by a bond between K835 and D848 (K817 and D830 in SARS-CoV FP). The equivalent residue in SARS-CoV FP, based on biological studies, is a critical residue [34]. Mutating D830 removes the binding partner of K817, thereby loosening the 'knot' of the structured FPPR in maintaining the closed form of the trimeric S protein [34]. Without the reinforcements, we may lose the optimal structural conformation of the S protein upon receptor binding to expose the S2' cleavage site to promote successful proteolytic cleavage [30].

More broadly, the E801 and D830 residues are conserved within the CoV family and the D812 residue is conserved within betacoronaviruses [18, 19]. The implication is that calcium interactions are a conserved mechanism that serves to better position the FP for membrane insertion. Different coronaviruses exhibit different requirements for calcium; MERS-CoV binds to one Ca^{2+} ion in its FP1 domain [20], thus, it is important to investigate the role of Ca^{2+} and FP interactions across the CoV family. The conservation of calcium-binding residues in the FP of many coronaviruses suggests that the CoV fusion mechanisms can be potential targets for broad-spectrum antiviral drugs [35-37]. Repurposing FDA-approved calcium channel blocking (CCB) drugs to inhibit CoV entry, particularly for SARS-CoV-2, is one option worth exploring. Recent studies have shown that the CCB felodipine is a potential candidate to inhibit SARS-CoV-2 entry [35]. CCBs can target conserved viral functions, providing a rapid solution to address new and future SARS-CoV-2 variants. It will be important to identify the mechanisms of CCBs CoV inhibition, as they may directly inhibit a viral target or indirectly inhibit viral entry by affecting host cell processes

In this study, we elucidate the relationship between highly conserved residues in the SARS CoV FP and the critical role they have in coordinating calcium binding to facilitate viral entry. Interestingly, SARS-CoV-2 variants have arisen as part of Clade 20A that contain a D839G or D839Y mutation (E821 equivalent in SARS-CoV), with this mutation predicted to affect FP-Ca^{2+} interactions [38-40]. To date, it is not known if there is any selective advantage to the virus conferred by this mutation or whether the emergence of these variants simply represents a founder effect.

Regarding to the role calcium plays during SARS-CoV entry, our data points to the necessity of intra- and extra-cellular calcium during infection. Loss of extracellular calcium results in a 50% reduction in PP infectivity, while the loss of intracellular calcium rendered pseudoparticles noninfectious. Together with the MD simulations, we propose a model of SARS-CoV viral entry mediated, in part, by calcium. In this model, upon S2' cleavage the spike protein's FP is exposed and stabilized by binding to 2 calcium ions through electrostatic interactions. We believe that the residues that likely mediate these essential interactions with calcium are E801/D802 and D812/E821. Stabilization of the FP is critical for host membrane insertion, given the unstructured and flexible FP2 loop in this peptide. We hypothesize that calcium interaction helps stabilize the FP structure prior to membrane insertion, thus in the absence of a single negatively charged residue, the FP can compensate through alternative residues to bind to calcium. Overall, more studies are needed to fully understand the role calcium plays in CoV FP function and its effects on viral pathogenesis.

Materials and Methods

565 **Cells, plasmids, and reagents.** Human embryonic kidney 293 (HEK293T) and African green
566 monkey kidney epithelial (VeroE6) cells were obtained from the American Type Culture
567 Collection (ATCC, Manassas, VA). Both cell lines were grown in complete DMEM, composed of
568 Dulbecco's modified Eagle medium (DMEM, CellGro), supplemented with 10% HyClone
569 FetalClone II (GE) and 10 mM HEPES (CellGro) at 37°C and 5% CO_2. The plasmids used for
570 generating pseudoparticles were the pCMV-MLV gag-pol murine leukemia virus (MLV) packaging
571 construct, the pTG-Luc transfer vector encoding the luciferase reporter gene, and the pCAGGS-
572 VSVG plasmids were provided by Jean Dubuisson (Lille Pasteur Institute, Lille, France) and co-
573 transfected as previously described [27]. The plasmid encoding the C9-tagged SARS-CoV spike
574 protein (pcDNA3.1-C9-SARS-CoV S) was provided by Dr. Michael Farzan from the New England
575 Primate Research Center. Recombinant L-1-tosylamide-2-phenylethyl chloromethyl ketone
576 (TPCK)-treated trypsin was obtained from Sigma. The calcium chelators EGTA and BAPTA-AM
577 (acetoxymethyl ester) were obtained from VWR and Tocris, respectively. Both compounds were
578 diluted in dimethyl sulfoxide (ThermoFisher) prior to use.
579
580 **Site-directed mutagenesis.** Site-directed mutagenesis was performed on the SARS-CoV spike
581 protein vector, pcDNA3.1-SARS-CoV-S, via the QuikChange Lightning site-directed mutagenesis
582 kit (Aligent). PCRs and transformations were performed based on the manufacturer's
583 recommendations. Primers obtained from IDT Technologies were designed using the primer
584 design tool from Aligent. The primers used to generate the SARS-CoV S mutants can be found in
585 the supplementary information (**SI, Table S1**). Mutations were confirmed via Sanger Sequencing
586 at the Cornell University Life Sciences Core Laboratories Center.

587

588 **Cell Surface Biotinylation Assay.** HEK293T cells were seeded at a density of 8×10^5 cells per well
589 in poly-D-lysine coated 6-well plates. 24 hours later, cells were transfected with 2ug of WT or
590 mutant SARS-CoV S protein expressing plasmids using polyethylenimine (PEI) (Fisher). To
591 transfect each well, 2 µg of plasmid DNA and 6 µL of a 1ug/uL solution of PEI were incubated with
592 50 µL of serum free OptiMEM (Gibco) for 20 minutes. 2 mL of complete DMEM were then added
593 to this transfection mixture, which was used to replace the cell media. Cells were transfected for
594 24 hours, washed once with 1X DPBS, and then left untreated or treated with 1mL of 0.8 nM
595 TPCK-trypsin in DPBS for 10 minutes at 37°C. Cell surface proteins were then biotinylated on ice
596 by incubating rinsed cells in a biotin-containing buffer (250 ug/mL in PBS) for 20 minutes. The
597 biotin buffer was then replaced with a quenching solution (50mM glycine in DPBS) and incubated
598 for 30 minutes on ice. Cells were then lysed for 15 minutes using a lysis buffer containing 0.1%
599 Triton in 1x TBS with protease inhibitors (cOmplete Protease Inhibitor Cocktail). Lysates were
600 collected and spun at 13000 rpm for 10 minutes to pellet the insoluble material. The lysates were
601 then incubated overnight at 4° C with equilibrated steptavidin beads to retrieve the biotinylated
602 spike proteins. The captured spike proteins were eluted by boiling the beads in 1x LDS sample
603 buffer in the presence of DTT (NuPAGE) for 10 minutes. Proteins were resolved on 4-12% gradient
604 Bis-Tris gels (NuPAGE) and transferred to PVDF membranes. The SARS-CoV S protein was
605 detected using the SARS-CoV S rabbit polyclonal primary antibody (NR-4569, BEI resources) and
606 Alexa Fluor 488-labeled goat anti-rabbit secondary antibody (Invitrogen). The resulting protein
607 bands were visualized using a Chemidoc system with Image Lab image capture software (BioRad).
608 Bands have only been adjusted in contrast and brightness using the Image Lab software.

609

610 **Cell-cell fusion assay.** 3.5 × 10^5 VeroE6 cells were seeded in 8-well chamber slides (Millipore).
611 After 24 hours, cells were transfected with a mixture containing 0.75 µL of Turbofect
612 (Thermofisher), 0.5 µg of S-expressing plasmid, and 11.75 µL OptiMEM for each well. Following
613 18 hours of transfection, cells were washed with 1X DPBS and trysinized with 0.8 nM TPCK-trypsin
614 for 5 minutes at 37°C to. Cells were then fixed with 4% paraformaldehyde (PFA) (ThermoFisher)
615 for 15 minutes and washed three times with DPBS. To permeabilize the cells, 0.1% Triton X-100
616 was added to each well and cells were incubated for 5 minutes on ice. After three washes with
617 DPBS, the cells were blocked with 5% normal goat serum for 30 minutes. Cells were again washed
618 and then labeled with SARS-CoV S rabbit polyclonal antibody (NR-4569, BEI resources), followed
619 by labeling with Alexa Fluor 488-labeled goat anti-rabbit secondary antibody (Invitrogen). The
620 cell nuclei were labeled with a DAPI stain present in the mounting media (DAPI Fluoromount-G,
621 Southern Biotech). Microscopy images were acquired using an upright microscope (Echo Revolve)
622 with a 10x objective. To quantify the number of nuclei per syncytia, three randomly selected
623 fields were acquired and spike-expressing cells and syncytia were manually counted. The average
624 number of nuclei per syncytium and standard deviation were calculated and visualized using
625 Microsoft Excel and GraphPad Prism 7.

626

627 **SARS CoV pseudoparticle infectivity assays.** SARS-CoV pseudoparticles were produced as
628 previously described [20, 27]. To generate pseudoparticles, 3.5 x10^5 HEK293T cells were seeded
629 in 6-well plates. Pseudoparticles were prepared by transfecting HEK293T cells with 600 µg of their
630 respective SARS WT or mutant S plasmids, 800 µg of pTG-Luc, and 600 µg of pCMV-MLV gagpol

using polyethylenimine (PEI) as the transfection reagent. The cell supernatant was harvested 48 hours post-transfection, centrifuged at 1200 rpm for 7 minutes to separate the pseudoparticles from residual cellular debris, and filtered through a 0.45 µm syringe filter. The pseudoparticles were stored at -80°C for one freeze-thaw cycle. To determine pseudoparticle infectivity, $5x10^5$ VeroE6 cells were seeded into 24-well plates and infected 200uL of pseudoparticles for 72 hrs at 37°C. Cells were lysed for 10 minutes at room temperature using the Luciferase cell lysis reagent (Promega). Luminescence readings were performed using a luminometer, Glomax 20/20 system (Promega). Each experiment contained three technical replicates and was repeated at least three times. Data analysis was performed using graphical software, GraphPad Prism 7.

For the calcium depletion studies, calcium was chelated from the extracellular or intracellular environment using EGTA or BAPTA-AM, respectively. To deplete extracellular calcium levels, VeroE6 cells were pre-treated with DMEM lacking calcium (DMEM- lacks L-glutamine, sodium pyruvate, HEPES, and calcium; it contains 2% HyClone and 10 mM HEPES) for 1 hour at 37°C. After the DMEM- pretreatment, the VeroE6 cells were infected with 200 µL of pseudoparticles in the presence of 50 µM EGTA for 2 hours at 37°C. Following infection, cells were supplemented with 300 µL of calcium-containing cDMEM.

To chelate intracellular calcium, VeroE6 cells were pretreated with 50 µM BAPTA-AM (dissolved in DMSO) in DMEM+ (DMEM without L-glutamine, sodium pyruvate, HEPES; 2% HyClone; 10 mM HEPES; Gibco) in the same conditions as described above. Cells were then infected with 200 µL of pseudoparticles in the presence of 50 µM BAPTA-AM for 2 hours and supplemented with cDMEM post-infection. Because BAPTA-AM was dissolved in DMSO, VeroE6 cells were pretreated with the equivalent percentage of DMSO used in the BAPTA-AM treated

cells. This served as an important control for the effects of DMSO alone on our infectivity assay. Pseudoparticles infections carried out in calcium-containing DMEM+ served as a positive control for infection in absence of the extracellular chelator. Analysis of pseudoparticle infectivity under these calcium depletion conditions was performed as described above.

To confirm the presence of the S protein in the pseudoparticles, 1.5 mL of the harvested pseudoparticles were spun down using an ultracentrifuge in a TLA-55 rotor (Beckman-Coulter) at 42,000 × *g* for 2 hours at 4°C. The supernatant was aspirated and the S protein-containing pellet was resuspended and boiled in 1x LDS sample buffer in the presence of DTT for 10 minutes. The samples were resolved and immunoblotted for the spike protein as described above.

Modeling of the SARS-CoV fusion peptide. The structural cartoon model of the SARS-CoV S protein fusion peptide is based on the SARS-CoV S prefusion structure from the Protein Data Bank, PDB 5XLR. The sequence of the SARS-CoV S protein (GenBank accession no. AAT74874.1) was aligned to the PDB 5XLR SARS-CoV structure sequence using Geneious software (**v.2020.1.1**). Structural models of the SARS-CoV S monomer were generated using the Modeller comparative modeling tool (**v.9.23**) within the Chimera software (v.1.13; University of California). Images were created using Adobe Illustrator CC (**v.24.03**).

Molecular dynamics (MD) simulations of the SARS-CoV FP in water. For all the atomistic MD simulations, the SARS-CoV FP segment was capped with neutral N- and C-termini (ACE and CT3, respectively, in the CHARMM force-field nomenclature). Protonation states of all the titratable residues were predicted at pH 7 using Propka 3.1 software [42].

675 For the simulations in water, one copy of the peptide (wild-type or a mutant) was embedded
676 in a rectangular solution box and ionized using VMD tools ("Add Solvation Box" and "Add Ions",
677 respectively) [43]. The box of dimensions ~90 Å x 80 Å x 82 Å included a Na^+Cl^- ionic solution as
678 well as 2 Ca^{2+} ions, and ~18000 water molecules. The total number of atoms in the system was
679 ~54,540.

680 The system was equilibrated with NAMD version 2.13 [44] following a multi-step protocol
681 during which the backbone atoms of the SARS-CoV FP as well as Ca^{2+} ions in the solution were
682 first harmonically constrained and subsequently gradually released in four steps (totaling ~3ns),
683 changing the restrain force constants k_F from 1, to 0.5, to 0.1 kcal/ (mol Å^2), and 0 kcal/ (mol Å^2).
684 These simulations implemented all option for rigidbonds, 1fs (for k_F 1, 0.5, and 0.1 kcal/ (mol Å^2))
685 or 2fs (for k_F of 0) integration time-step, PME for electrostatics interactions [45], and were carried
686 out in NPT ensemble under isotropic pressure coupling conditions, at a temperature of 310 K.
687 The Nose-Hoover Langevin piston algorithm [46] was used to control the target P = 1 atm
688 pressure with the "LangevinPistonPeriod" set to 200 fs and "LangevinPistonDecay" set to 50 fs.
689 The van der Waals interactions were calculated applying a cutoff distance of 12 Å and switching
690 the potential from 10 Å.

691 After this initial equilibration phase, the velocities of all atoms in the system were reset and
692 ensemble MD runs were initiated with OpenMM version 7.4 [47] during which the system was
693 simulated in 18 independent replicates, each for 640ns (i.e., cumulative time of ~11.5 µs for each
694 FP construct). These runs implemented PME for electrostatic interactions and were performed
695 at 310K temperature under NVT ensemble. In addition, 4fs time-step was used, with hydrogen
696 mass repartitioning and with "friction" parameter set to 1.0/picosecond. Additional parameters

for these runs included: "EwaldErrorTolerance" 0.0005, "rigidwater" True, and "ConstraintTolerance" 0.000001. The van der Waals interactions were calculated applying a cutoff distance of 12 Å and switching the potential from 10 Å.

MD simulations of SARS-CoV FP interactions with lipid membranes. Interactions of selected two models of the Ca^{2+}-bound WT SARS-CoV FP with lipid membranes were investigated with atomistic MD simulations. These runs were initiated by placing each of the models in the proximity of a bilayer composed of 3:1:1 POPC/POPG/Cholesterol that had been pre-equilibrated for 25ns as described previously [23].

After the FP-membrane complexes were embedded in a solution box (containing 150 mM Na^+Cl^- salt concentration), each system was equilibrated with NAMD version 2.13 following the same multi-step protocol described above during which the backbone atoms of the FP as well as the Ca^{2+} ions were first harmonically constrained and subsequently gradually released in four steps. After this phase, the velocities of all atoms of the system were reset, and ensemble MD runs were initiated with OpenMM version 7.4. Each system was simulated in 18 independent replicates, each ran for ~ 1 μs (i.e., cumulative time of ~18 μs for each FP-membrane complex). These runs implemented PME for electrostatic interactions and were performed at 298K temperature under NPT ensemble using semi-isotropic pressure coupling, with 4fs time-steps, using hydrogen mass repartitioning and with "friction" parameter set to 1.0/picosecond. Additional parameters for these runs included: "EwaldErrorTolerance" 0.0005, "rigidwater" True, and "ConstraintTolerance" 0.000001. The van der Waals interactions were calculated applying a cutoff distance of 12 Å and switching the potential from 10 Å.

719 For all simulations we used the latest CHARMM36 force-field for proteins and lipids [48], as well
720 as the recently revised CHARMM36 force-field for ions which includes non-bonded fix (NBFIX)
721 parameters for Na^+ and Ca^{2+} ions [49].

722

723 ## Acknowledgements

724 This work was supported by The National Institute of Health research grant R01AI35270, National
725 Science Foundation RAPID grant 2027070 and Fast Grant from the Mercatus Center at George
726 Mason University. TT is supported by the National Science Foundation Graduate Research
727 Fellowship Program under Grant No. DGE-1650441 and the Samuel C. Fleming Family Graduate
728 Fellowship. We would like to thank members of the Daniel, Whittaker, and Abbott groups as well
729 as the Weinstein group at Weill Cornell for helpful discussions.

730

731 ## Author Contributions

732 Conceived and designed the experiments: MKB GK MRS HW GRW SD. Performed the
733 experiments: MKB GK MRS TT JDC. Analyzed the data: MKB GK MRS TT HW GRW SD JDC. Wrote
734 and edited the paper: MKB GK MRS TT HW GRW SD JDC. Acquired funding: GRW SD.

735

736

Figure 1. Generating the charge-to-alanine mutations in the SARS-CoV fusion peptide. (A) The predicted structure of the SARS-CoV fusion peptide (FP) modeled on the SARS PDB: 5XLR. (B) The sequence of the wild-type (WT) SARS FP showing all 40 amino acids (GenBank accession no. AAT74874.1) Listed below are the single charge-to-alanine mutations generated in the aspartic (D) and glutamic (E) acids. The red charged WT residues and the green substitution are shown in each position for the single mutants. Gold highlights a critical disulfide bond within the FP that is necessary for its function. (C) Alignment of the amino acid sequences of SARS-CoV, MERS-CoV, and SARS-CoV-2 FPs showing the high conservation of the LLF motif (green), the charges residues (red) and the disulfide bond. Note that the green LLF residues were not mutated in this study.

Figure 2. Cleavage comparison of SARS-CoV wild-type and mutant spike. Western blot analysis of WT and mutant S proteins with (*+*) and without (-) trypsin. S_0 indicates the full-length, uncleaved spike protein. S_2 indicates the cleaved S2 subunit of the spike protein. (A) Spike immunoblots showing the accumulation of WT S and single charge-to-alanine mutants. (B) Spike immunoblots showing the additional mutants generated at the E801 position. N = 4 (biological replicates).

Figure 3. Fusion activity of the SARS-CoV wild-type and mutant S-expressing cells. (A) Representative immunofluorescence images of VeroE6 cells expressing WT or mutant D802A S constructs. Following transfection, cells were treated with trypsin to cleave SARS-CoV S proteins and induce syncytium formation. Syncytia were visualized using a SARS-CoV S antibody (*green*) and nuclei appear in blue (DAPI). Images were taken at 10X magnification. Scale bars =170µM (B) Quantification of nuclei per syncytium. *** denotes significance of $p < 0.001$; **** denotes significance of $p < 0.0001$.

Figure 4. Infectivity of wild-type and mutant SARS-CoV pseudoparticles. (A) Spike immunoblots of pseudoparticles containing wild-type and mutant spike. S_0 indicates the full-length, uncleaved spike protein. S_2 indicates the cleaved S2 subunit of the spike protein. (B) WT and mutant SARS-CoV pseudoparticle infectivity in VeroE6 cells treated with 50 µM EGTA (+) or left untreated (-). (C) WT and mutant SARS-CoV pseudoparticle infectivity in VeroE6 cells treated with 50 µM BAPTA-AM (+) or left untreated (-). * denotes significance of $p < 0.05$; ** denotes significance of $p < 0.01$; *** denotes significance of $p < 0.001$; **** denotes significance of $p < 0.0001$.

Figure 5. Assessing the potential redundancy in fusion peptide and calcium interactions (A) Double and triple mutants were generated in the FP to determine if residues E821 and D825 are functionally redundant. Multiple charged residues (red) in the SARS FP were mutated to alanines (green) to generate double and triple mutants. Gold highlights a critical disulfide bond within the FP that is necessary for its function. (B) Western blot analysis of WT and double/ triple mutant S proteins with (*+*) and without (-) trypsin. S_0 indicates the full-length, uncleaved spike protein. S_2 indicates the cleaved S2 subunit of the spike protein.

(C) Representative immunofluorescence images of VeroE6 cells expressing WT or the triple mutant (E821A/D825A/D830A) S constructs. Following transfection, cells were treated with

trypsin to cleave SARS-CoV S proteins and induce syncytium formation. Syncytia were visualized using a SARS-CoV S antibody (*green*) and nuclei appear in blue (DAPI). Images were taken at 10X magnification. Scale bars =170µM (D) Quantification of nuclei per syncytium in the WT and double/triple mutant expressing VeroE6 cells. (E) Spike immunoblots of pseudoparticles containing wild-type and double/triple mutant spike. S_0 indicates the full-length, uncleaved spike protein. S_2 indicates the cleaved S2 subunit of the spike protein. (F) WT and double/triple mutant SARS-CoV pseudoparticle infectivity in VeroE6 cells treated with 50 µM EGTA (+) or left untreated (-). (G) WT and double/triple mutant SARS-CoV pseudoparticle infectivity in VeroE6 cells treated with 50 µM BAPTA-AM (+) or left untreated (-). * denotes significance of $p < 0.05$; *** denotes significance of $p < 0.001$; **** denotes significance of $p < 0.0001$.

Figure 6. Modes of Ca^{2+} binding to SARS-CoV fusion peptide. Number of Ca^{2+} binding events to different pairs of anionic residues in SARS-CoV FP in the simulations of the WT and the mutant constructs (labeled in each panel). The experimentally measured phenotypes for each construct are shown (active or inactive). The mode of Ca^{2+} ion association predicted to be inhibitory for membrane insertion (E821-D825) is shown in *red*, and the modes of Ca^{2+} association predicted to facilitate membrane insertion are depicted in *green*.

Figure 7. Membrane insertion for FP1 and FP2 domains of SARS-CoV fusion peptide. (A-B) Frequency of membrane insertion for each residue of SARS-CoV FP in the MD simulations of Model 1 (A) and Model 2 (B) constructs (differing in the mode of Ca^{2+} coordination, see text). The snapshot insertions in the panels show the corresponding structures. Ca^{2+} coordinating anionic residues are highlighted by licorice rendering; Ca^{2+} ions are shown as blue spheres. The FP1 and FP2 parts of the fusion peptide are colored in silver and lime, respectively. (C-D) The same frequency calculations but done separately for two representative trajectories in Model 1 set in which the observed membrane insertions involved the N-terminal LLF motif (C) and the more centrally located (F815-M816) hydrophobic segment (D). The corresponding snapshots illustrate structural features of these two distinct insertion modes highlighting (in licorice) positions of the anionic residues, the hydrophobic residues penetrating the membrane, and R829 residue interacting with D825. Same color code as in panels A-B.

Figure 8. Predicted model of CoV FP interaction with a lipid bilayer. This model is based on the pre-fusion FP domain (from PDB: 5XLR), and summarizes the data obtained from our work, highlighting the role of key charged residues within the fusion peptide. We depict the insertion of the FP1 domain with E801/D802-Ca^{2+} (green) needed for membrane association and with D812 able to coordinate Ca^{2+} and pair with either E821 to promote membrane interaction (green) or with D825 to inhibit membrane interaction (red).

References

1. Lai MMC, Cavanagh D. The Molecular Biology of Coronaviruses. Elsevier; 1997. p. 1-100.
2. Masters PS. The Molecular Biology of Coronaviruses. Advances in Virus Research2006. p. 193-292.
3. Cherry JD, Krogstad P. SARS: the first pandemic of the 21st century. Pediatr Res. 2004;56(1):1-5. Epub 2004/05/21. doi: 10.1203/01.PDR.0000129184.87042.FC. PubMed PMID: 15152053; PubMed Central PMCID: PMCPMC7086556.
4. de Groot RJ, Baker SC, Baric RS, Brown CS, Drosten C, Enjuanes L, et al. Middle East respiratory syndrome coronavirus (MERS-CoV): announcement of the Coronavirus Study Group. J Virol. 2013;87(14):7790-2. Epub 2013/05/17. doi: 10.1128/JVI.01244-13. PubMed PMID: 23678167; PubMed Central PMCID: PMCPMC3700179.
5. Wu F, Zhao S, Yu B, Chen YM, Wang W, Song ZG, et al. A new coronavirus associated with human respiratory disease in China. Nature. 2020;579(7798):265-9. Epub 2020/02/06. doi: 10.1038/s41586-020-2008-3. PubMed PMID: 32015508; PubMed Central PMCID: PMCPMC7094943.
6. Zhou P, Yang XL, Wang XG, Hu B, Zhang L, Zhang W, et al. A pneumonia outbreak associated with a new coronavirus of probable bat origin. Nature. 2020;579(7798):270-3. Epub 2020/02/06. doi: 10.1038/s41586-020-2012-7. PubMed PMID: 32015507; PubMed Central PMCID: PMCPMC7095418.
7. M SM, P M, F A-S, C R, MP K, B M. World Health Organization methodology to prioritize emerging infectious diseases in need of research and development. Emerg Infect Dis. 2018. doi: 10.3201/eid2409.171427.
8. da Costa VG, Moreli ML, Saivish MV. The emergence of SARS, MERS and novel SARS-2 coronaviruses in the 21st century. Arch Virol. 2020;165(7):1517-26. Epub 2020/04/22. doi: 10.1007/s00705-020-04628-0. PubMed PMID: 32322993.
9. Velavan TP, Meyer CG. The COVID-19 epidemic. Trop Med Int Health. 2020;25(3):278-80. Epub 2020/02/16. doi: 10.1111/tmi.13383. PubMed PMID: 32052514.
10. Tang T, Bidon M, Jaimes JA, Whittaker GR, Daniel S. Coronavirus membrane fusion mechanism offers a potential target for antiviral development. Antiviral Res. 2020;178:104792. Epub 2020/04/10. doi: 10.1016/j.antiviral.2020.104792. PubMed PMID: 32272173; PubMed Central PMCID: PMCPMC7194977.
11. de Wit E, van Doremalen N, Falzarano D, Munster VJ. SARS and MERS: recent insights into emerging coronaviruses. Nat Rev Microbiol. 2016;14(8):523-34. Epub 2016/06/28. doi: 10.1038/nrmicro.2016.81. PubMed PMID: 27344959.
12. Belouzard S, Millet JK, Licitra BN, Whittaker GR. Mechanisms of coronavirus cell entry mediated by the viral spike protein. Viruses. 2012;4(6):1011-33. Epub 2012/07/21. doi: 10.3390/v4061011. PubMed PMID: 22816037; PubMed Central PMCID: PMCPMC3397359.
13. Millet JK, Whittaker GR. Physiological and molecular triggers for SARS-CoV membrane fusion and entry into host cells. Virology. 2018;517:3-8. Epub 2017/12/26. doi: 10.1016/j.virol.2017.12.015. PubMed PMID: 29275820.
14. Lee C-Y, Lowen AC. Animal models for SARS-CoV-2. Current Opinion in Virology. 2021;48:73-81. doi: 10.1016/j.coviro.2021.03.009.

15. Millet JK, Whittaker GR. Host cell proteases: Critical determinants of coronavirus tropism and pathogenesis. Virus Res. 2015;202:120-34. Epub 2014/12/03. doi: 10.1016/j.virusres.2014.11.021. PubMed PMID: 25445340; PubMed Central PMCID: PMCPMC4465284.
16. Stevens CS, Oguntuyo KY, Benhur L. Proteases and variants: context matters for SARS-CoV-2 entry assays. Current Opinion in Virology. 2021. doi: 10.1016/j.coviro.2021.07.004.
17. White JM, Whittaker GR. Fusion of Enveloped Viruses in Endosomes. Traffic. 2016;17(6):593-614. Epub 2016/03/05. doi: 10.1111/tra.12389. PubMed PMID: 26935856; PubMed Central PMCID: PMCPMC4866878.
18. Madu IG, Roth SL, Belouzard S, Whittaker GR. Characterization of a highly conserved domain within the severe acute respiratory syndrome coronavirus spike protein S2 domain with characteristics of a viral fusion peptide. J Virol. 2009;83(15):7411-21. Epub 2009/05/15. doi: 10.1128/JVI.00079-09. PubMed PMID: 19439480; PubMed Central PMCID: PMCPMC2708636.
19. Lai AL, Millet JK, Daniel S, Freed JH, Whittaker GR. The SARS-CoV Fusion Peptide Forms an Extended Bipartite Fusion Platform that Perturbs Membrane Order in a Calcium-Dependent Manner. J Mol Biol. 2017;429(24):3875-92. Epub 2017/10/24. doi: 10.1016/j.jmb.2017.10.017. PubMed PMID: 29056462; PubMed Central PMCID: PMCPMC5705393.
20. Straus MR, Tang T, Lai AL, Flegel A, Bidon M, Freed JH, et al. Ca(2+) Ions Promote Fusion of Middle East Respiratory Syndrome Coronavirus with Host Cells and Increase Infectivity. J Virol. 2020;94(13). Epub 2020/04/17. doi: 10.1128/JVI.00426-20. PubMed PMID: 32295925; PubMed Central PMCID: PMCPMC7307142.
21. Nathan L, Lai AL, Millet JK, Straus MR, Freed JH, Whittaker GR, et al. Calcium Ions Directly Interact with the Ebola Virus Fusion Peptide To Promote Structure-Function Changes That Enhance Infection. ACS Infect Dis. 2020;6(2):250-60. Epub 2019/11/21. doi: 10.1021/acsinfecdis.9b00296. PubMed PMID: 31746195; PubMed Central PMCID: PMCPMC7040957.
22. Lai AL, Freed JH. SARS-CoV-2 Fusion Peptide has a Greater Membrane Perturbating Effect than SARS-CoV with Highly Specific Dependence on Ca2+. Journal of Molecular Biology. 2021;433(10):166946.
23. Khelashvili G, Plante A, Doktorova M, Weinstein H. Ca²⁺-dependent mechanism of membrane insertion and destabilization by the SARS-CoV-2 fusion peptide. Biophysical Journal. 2021;120(6):1105-19. doi: 10.1016/j.bpj.2021.02.023.
24. Basso LG, Vicente EF, Crusca E, Jr., Cilli EM, Costa-Filho AJ. SARS-CoV fusion peptides induce membrane surface ordering and curvature. Sci Rep. 2016;6:37131. Epub 2016/11/29. doi: 10.1038/srep37131. PubMed PMID: 27892522; PubMed Central PMCID: PMCPMC5125003.
25. Koppisetti RK, Fulcher YG, Van Doren SR. Fusion Peptide of SARS-CoV-2 Spike Rearranges into a Wedge Inserted in Bilayered Micelles. Journal of the American Chemical Society. 2021. doi: 10.1021/jacs.1c05435.
26. Wang H, Yang P, Liu K, Guo F, Zhang Y, Zhang G, et al. SARS coronavirus entry into host cells through a novel clathrin- and caveolae-independent endocytic pathway. Cell Res. 2008;18(2):290-301. Epub 2008/01/30. doi: 10.1038/cr.2008.15. PubMed PMID: 18227861; PubMed Central PMCID: PMCPMC7091891.

27. Millet JK, Tang T, Nathan L, Jaimes JA, Hsu HL, Daniel S, et al. Production of Pseudotyped Particles to Study Highly Pathogenic Coronaviruses in a Biosafety Level 2 Setting. J Vis Exp. 2019;(145). Epub 2019/03/19. doi: 10.3791/59010. PubMed PMID: 30882796.
28. Tang T, Jaimes JA, Bidon MK, Straus MR, Daniel S, Whittaker GR. Proteolytic Activation of SARS-CoV-2 Spike at the S1/S2 Boundary: Potential Role of Proteases beyond Furin. ACS Infect Dis. 2021;7(2):264-72. Epub 2021/01/13. doi: 10.1021/acsinfecdis.0c00701. PubMed PMID: 33432808; PubMed Central PMCID: PMCPMC7839419.
29. Madu IG, Belouzard S, Whittaker GR. SARS-coronavirus spike S2 domain flanked by cysteine residues C822 and C833 is important for activation of membrane fusion. Virology. 2009;393(2):265-71. Epub 2009/09/01. doi: 10.1016/j.virol.2009.07.038. PubMed PMID: 19717178; PubMed Central PMCID: PMCPMC3594805.
30. Du L, He Y, Zhou Y, Liu S, Zheng BJ, Jiang S. The spike protein of SARS-CoV--a target for vaccine and therapeutic development. Nat Rev Microbiol. 2009;7(3):226-36. Epub 2009/02/10. doi: 10.1038/nrmicro2090. PubMed PMID: 19198616; PubMed Central PMCID: PMCPMC2750777.
31. Lu G, Wang Q, Gao GF. Bat-to-human: spike features determining 'host jump' of coronaviruses SARS-CoV, MERS-CoV, and beyond. Trends Microbiol. 2015;23(8):468-78. Epub 2015/07/25. doi: 10.1016/j.tim.2015.06.003. PubMed PMID: 26206723.
32. Dubé M, Rey FA, Kielian M. Rubella Virus: First Calcium-Requiring Viral Fusion Protein. PLOS Pathogens. 2014;10(12):e1004530. doi: 10.1371/journal.ppat.1004530.
33. Schaefer SL, Jung H, Hummer G. Binding of SARS-CoV-2 Fusion Peptide to Host tmpr and Plasma Membrane. The Journal of Physical Chemistry B. 2021;125(28):7732-41. doi: 10.1021/acs.jpcb.1c04176.
34. Cai Y, Zhang J, Xiao T, Peng H, Sterling SM, Walsh RM, et al. Distinct conformational states of SARS-CoV-2 spike protein. Science. 2020;369(6511):1586. doi: 10.1126/science.abd4251.
35. Straus MR, Bidon M, Tang T, Whittaker GR, Daniel S. FDA approved calcium channel blockers inhibit SARS-CoV-2 infectivity in epithelial lung cells. bioRxiv. 2020:2020.07.21.214577. doi: 10.1101/2020.07.21.214577.
36. Crespi B, Alcock J. Conflicts over calcium and the treatment of COVID-19. Evolution, Medicine, and Public Health. 2021;9(1):149-56. doi: 10.1093/emph/eoaa046.
37. Danta CC. Calcium Channel Blockers: A Possible Potential Therapeutic Strategy for the Treatment of Alzheimer's Dementia Patients with SARS-CoV-2 Infection. ACS Chem Neurosci. 2020;11(15):2145-8. Epub 2020/07/15. doi: 10.1021/acschemneuro.0c00391. PubMed PMID: 32662982.
38. Borges V, Isidro J, Cortes-Martins H, Duarte S, Vieira L, Leite R, et al. Massive dissemination of a SARS-CoV-2 Spike Y839 variant in Portugal. Emerging Microbes & Infections. 2020;9(1):2488-96. doi: 10.1080/22221751.2020.1844552.
39. Korber B, Fischer WM, Gnanakaran S, Yoon H, Theiler J, Abfalterer W, et al. Tracking Changes in SARS-CoV-2 Spike: Evidence that D614G Increases Infectivity of the COVID-19 Virus. Cell. 2020;182(4):812-27.e19.
40. Li Q, Wu J, Nie J, Zhang L, Hao H, Liu S, et al. The Impact of Mutations in SARS-CoV-2 Spike on Viral Infectivity and Antigenicity. Cell. 2020;182(5):1284-94.e9.

41. Belouzard S, Chu VC, Whittaker GR. Activation of the SARS coronavirus spike protein via sequential proteolytic cleavage at two distinct sites. Proceedings of the National Academy of Sciences. 2009;106(14):5871. doi: 10.1073/pnas.0809524106.
42. Olsson MHM, Søndergaard CR, Rostkowski M, Jensen JH. PROPKA3: Consistent Treatment of Internal and Surface Residues in Empirical pKa Predictions. Journal of Chemical Theory and Computation. 2011;7(2):525-37. doi: 10.1021/ct100578z.
43. Humphrey W, Dalke A, Schulten K. VMD: Visual molecular dynamics. Journal of Molecular Graphics. 1996;14(1):33-8.
44. Phillips JC, Braun R, Wang W, Gumbart J, Tajkhorshid E, Villa E, et al. Scalable molecular dynamics with NAMD. Journal of Computational Chemistry. 2005;26(16):1781-802.
45. Essmann U, Perera L, Berkowitz ML, Darden T, Lee H, Pedersen LG. A smooth particle mesh Ewald method. The Journal of Chemical Physics. 1995;103(19):8577-93. doi: 10.1063/1.470117.
46. Evans DJ, Holian BL. The Nose–Hoover thermostat. The Journal of Chemical Physics. 1985;83(8):4069-74. doi: 10.1063/1.449071.
47. Eastman P, Swails J, Chodera JD, McGibbon RT, Zhao Y, Beauchamp KA, et al. OpenMM 7: Rapid development of high performance algorithms for molecular dynamics. PLOS Computational Biology. 2017;13(7):e1005659. doi: 10.1371/journal.pcbi.1005659.
48. Huang J, Rauscher S, Nawrocki G, Ran T, Feig M, de Groot BL, et al. CHARMM36m: an improved force field for folded and intrinsically disordered proteins. Nature Methods. 2017;14(1):71-3. doi: 10.1038/nmeth.4067.
49. Venable RM, Luo Y, Gawrisch K, Roux B, Pastor RW. Simulations of Anionic Lipid Membranes: Development of Interaction-Specific Ion Parameters and Validation Using NMR Data. The Journal of Physical Chemistry B. 2013;117(35):10183-92. doi: 10.1021/jp401512z.

Figures

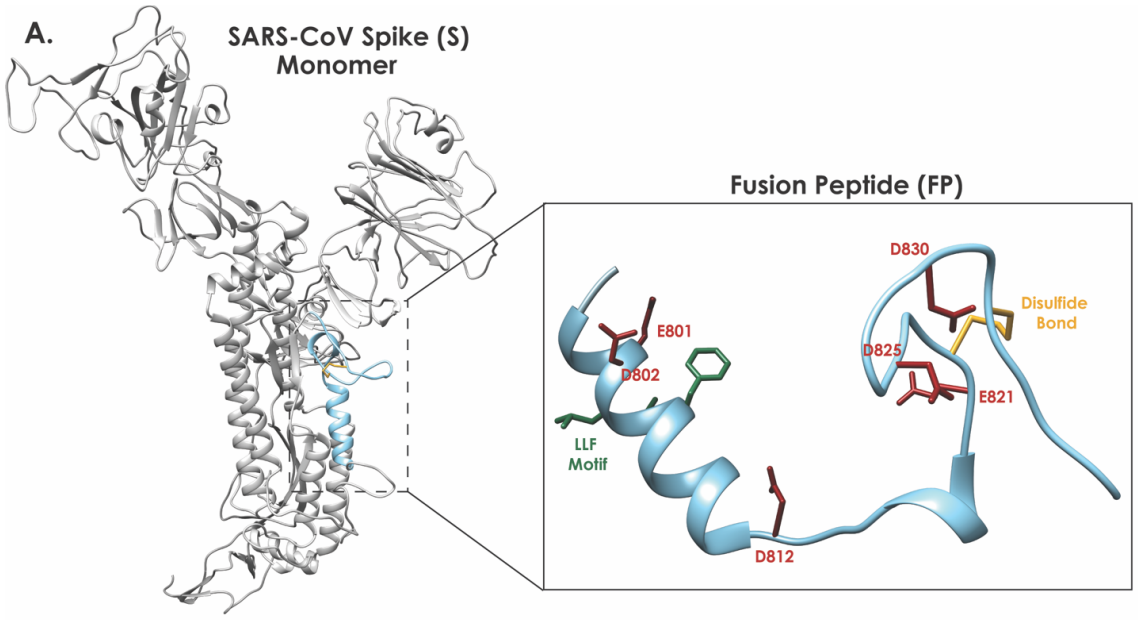

B.

WT	798–	SFIEDLLFNKVTLADAGFMKQYGECLGDINARDLICAQKF –837
		Disulfide Bond
E801A	798–	SFIADLLFNKVTLADAGFMKQYGECLGDINARDLICAQKF –837
D802A	798–	SFIEALLFNKVTLADAGFMKQYGECLGDINARDLICAQKF –837
D812A	798–	SFIEDLLFNKVTLAAAGFMKQYGECLGDINARDLICAQKF –837
E821A	798–	SFIEDLLFNKVTLADAGFMKQYGACLGDINARDLICAQKF –837
D825A	798–	SFIEDLLFNKVTLADAGFMKQYGECLGAINARDLICAQKF –837
D830A	798–	SFIEDLLFNKVTLADAGFMKQYGECLGDINARALICAQKF –837
		Disulfide Bond

C.

SARS-CoV	798–	SFIEDLLFNKVTLADAGFMKQYGECLG-DINARDLICAQKF –837
MERS-CoV	888–	SAIEDLLFDKVTIADPGYMQGYDDCMQQPASARDLICAQYV –929
SARS-CoV-2	816–	SFIEDLLFNKVTLADAGFIKQYGDCLG-DIAARDLICAQKF –855
		Disulfide Bond

Figure 1.

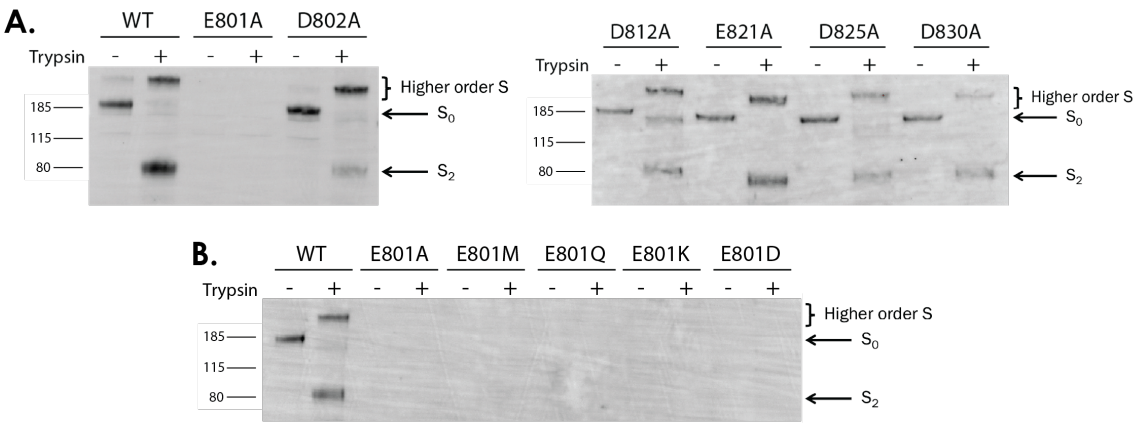

978

979

980 **Figure 2.**

981

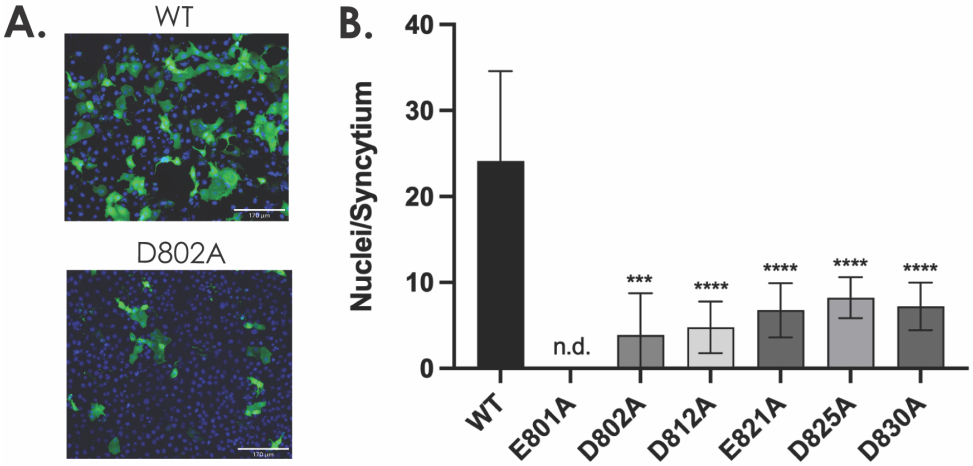

982

983 **Figure 3.**

984

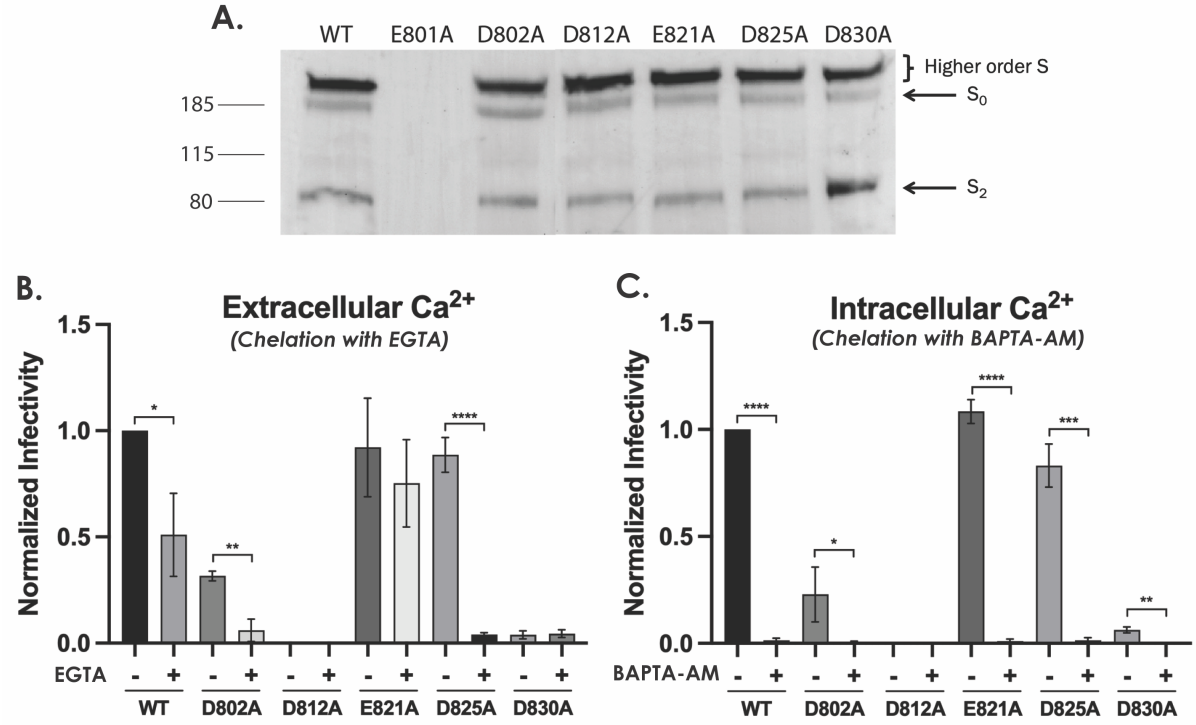

985

986 **Figure 4.**

987

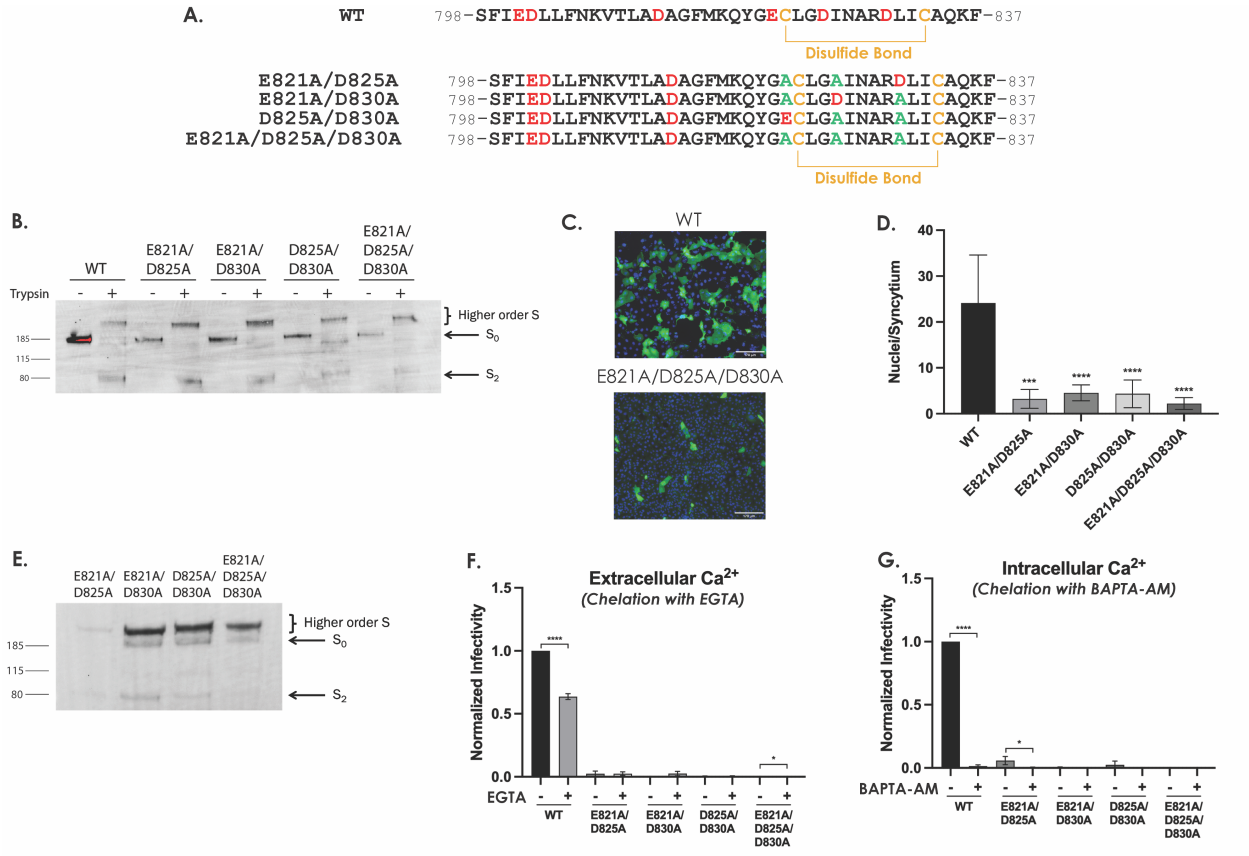

988

989 **Figure 5.**

990

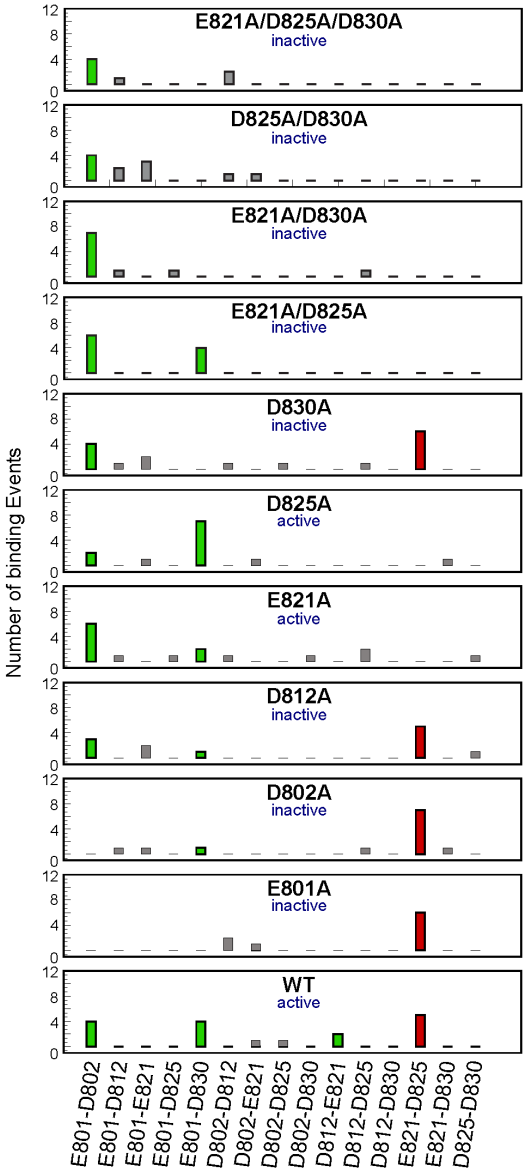

991

992 **Figure 6.**

993

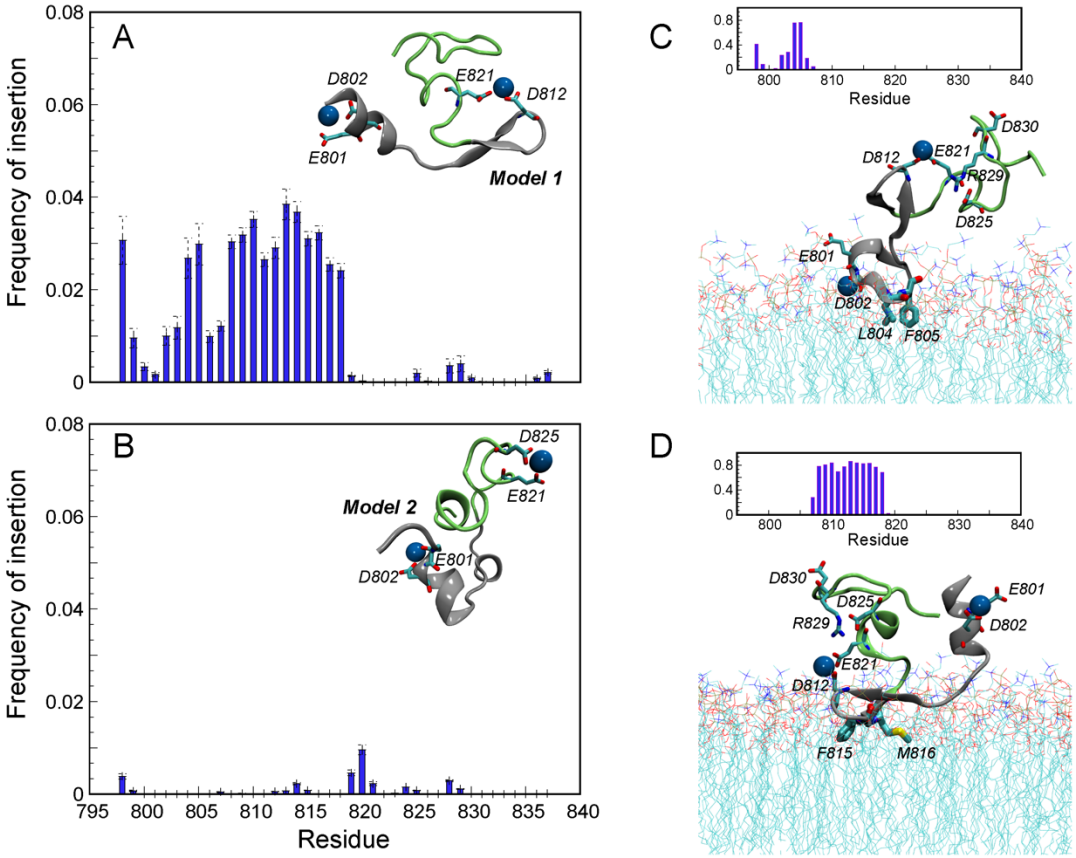

994

995 **Figure 7.**

996

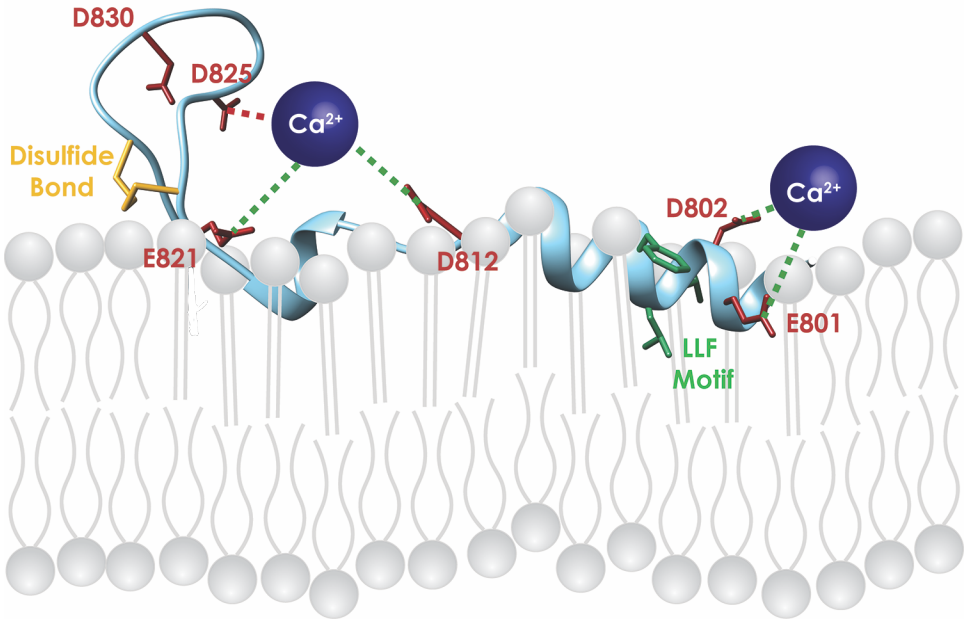

Figure 8.

Supplementary Information

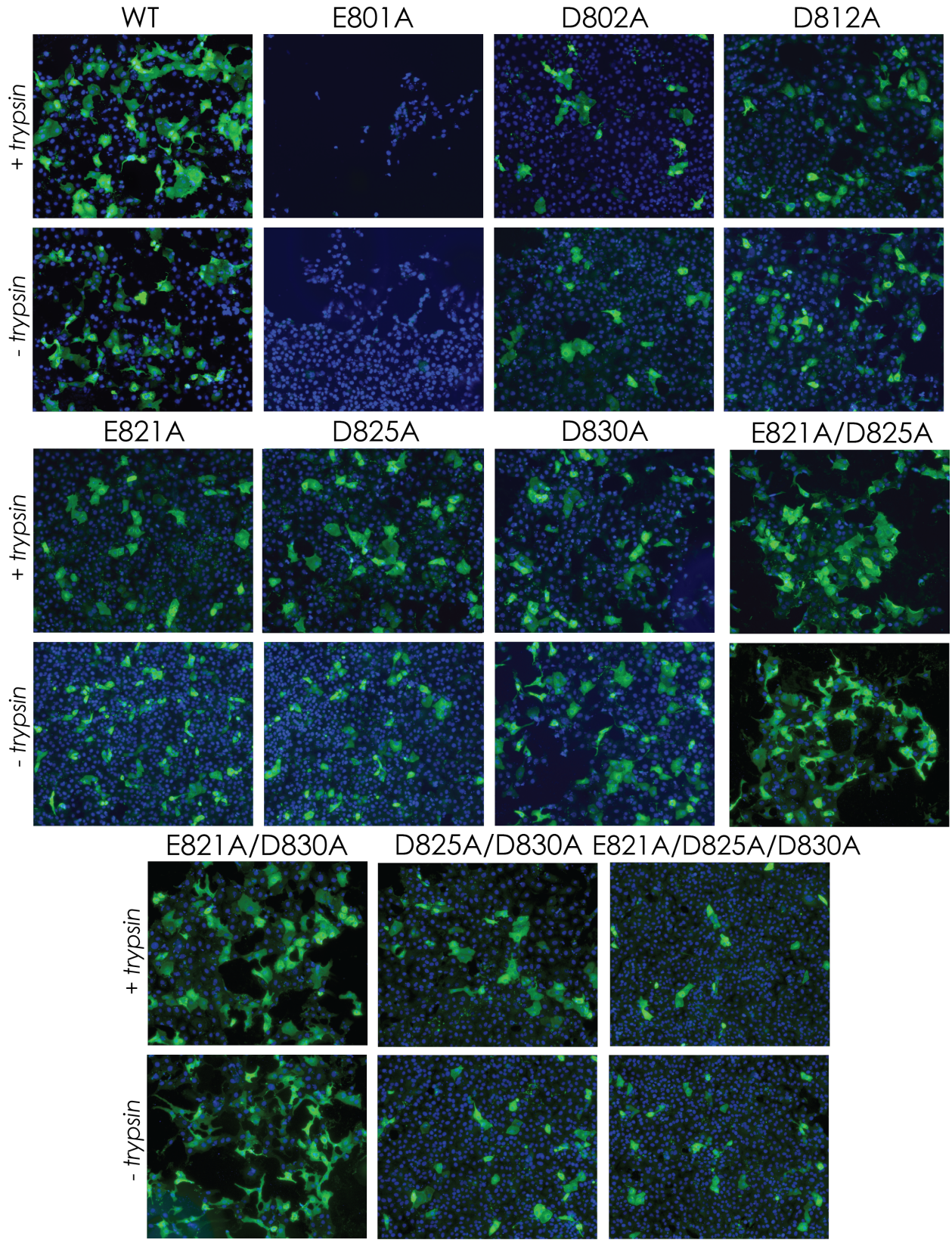

1001

SI Fig S1. Fusion activity of the SARS-CoV wild-type and mutant S-expressing cells. Immunofluorescence images of VeroE6 cells expressing WT or mutant (single/double/triple) S constructs. Following transfection, cells were treated with trypsin to cleave SARS-CoV S proteins and induce syncytium formation. Syncytia were visualized using a SARS-CoV S antibody (*green*) and nuclei appear in blue (DAPI). Images were taken at 10X magnification.

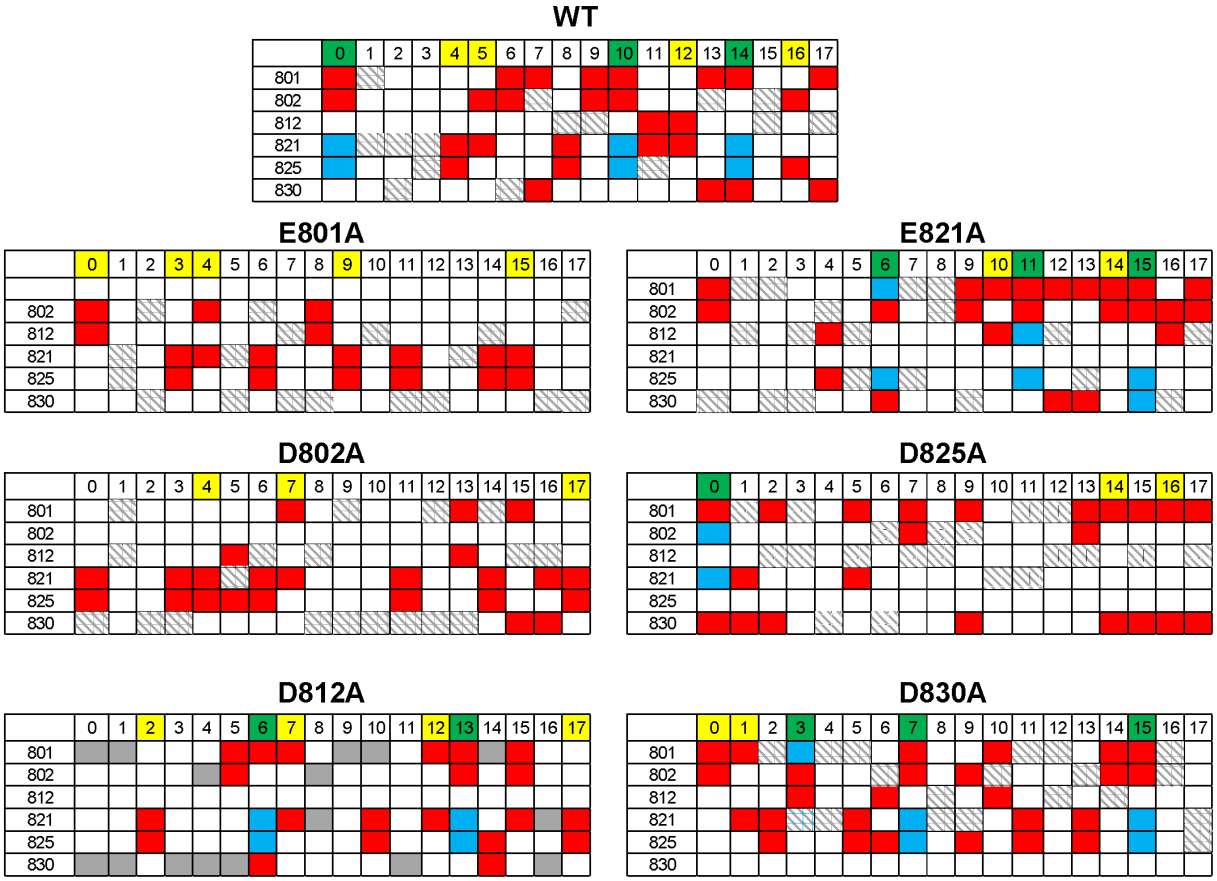

SI Fig S2. Models of Ca^{2+} binding to the WT and single mutant SARS-CoV FPs. The tables show, for each construct, acidic residues implicated in Ca^{2+} binding in 18 independent atomistic MD simulations (each 640ns in length). In a particular trajectory, residue pairs simultaneously engaging with the bound Ca^{2+} are denoted by *red* or *blue* rectangles, whereas instances of Ca^{2+} ion associating with a single acidic residue is depicted with *grey-striped* rectangle. The trajectories in which simultaneous binding of two Ca^{2+} ions to different pairs of residues were observed are highlighted in *green*. The simulations in which a single Ca^{2+} ion was bound to a pair of acidic residues are shown in *yellow*.

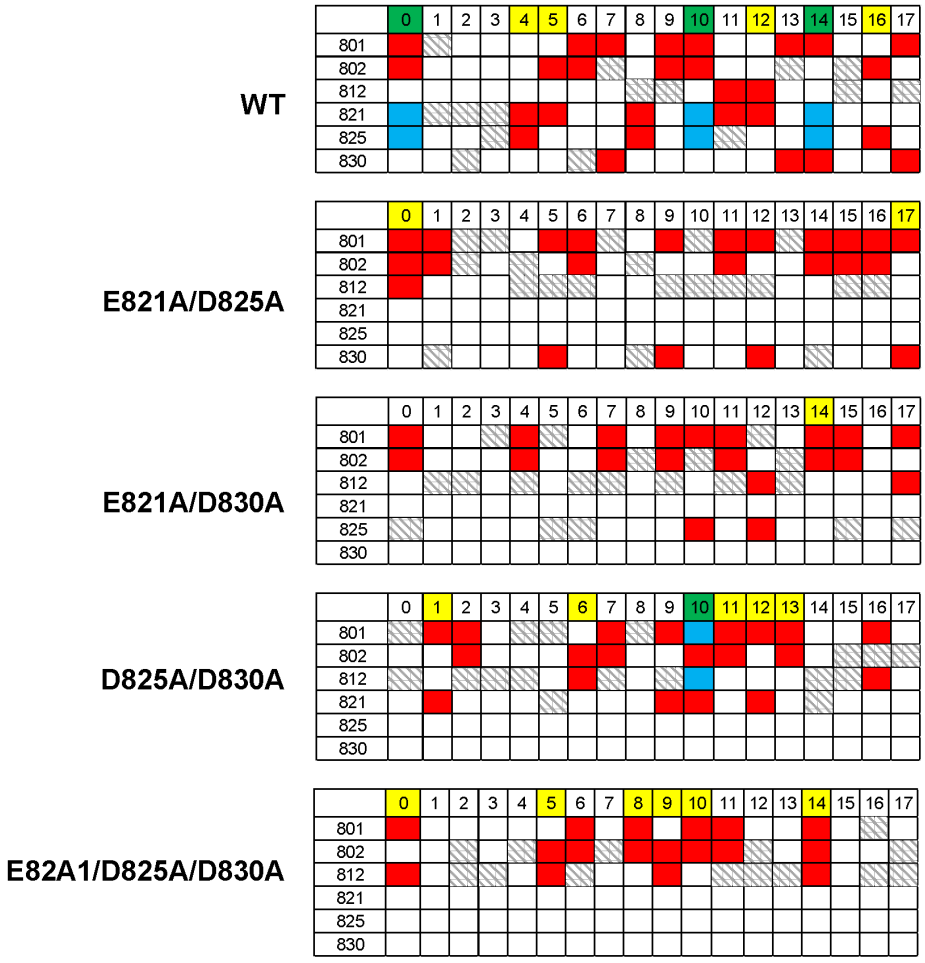

SI Fig S3. Models of Ca^{2+} binding to the WT and multiple mutant SARS-CoV FPs. The tables show, for each construct, acidic residues implicated in Ca^{2+} binding in 18 independent atomistic MD simulations (each 640ns in length). In a particular trajectory, residue pairs simultaneously engaging with the bound Ca^{2+} are denoted by *red* or *blue* rectangles, whereas instances of Ca^{2+} ion associating with a single acidic residue is depicted with *grey-striped* rectangle. The trajectories in which simultaneous binding of two Ca^{2+} ions to different pairs of residues were observed are highlighted in *green*. The simulations in which a single Ca^{2+} ion was bound to a pair of acidic residues are shown in *yellow*.

Mutation	Forward Primer	Reverse Primer
E801A	GCGCAGCTTCATCGCGGACCTGCTCTTCA	TGAAGAGCAGGTCCGCGATGAAGCTGCGC
E801M	TGTTGAAGAGCAGGTCCATGATGAAGCTGCGCTTGG	CCAAGCGCAGCTTCATCATGGACCTGCTCTTCAACA
E801Q	GAAGAGCAGGTCCTGGATGAAGCTGCGCT	AGCGCAGCTTCATCCAGGACCTGCTCTTC
E801K	TTGAAGAGCAGGTCCTTGATGAAGCTGCGCTTG	CAAGCGCAGCTTCATCAAGGACCTGCTCTTCAA
E801D	GTTGAAGAGCAGGTCGTCGATGAAGCTGCGC	GCGCAGCTTCATCGACGACCTGCTCTTCAAC
D802A	CTTGTTGAAGAGCAGGGCCTCGATGAAGCTGCG	CGCAGCTTCATCGAGGCCCTGCTCTTCAACAAG
D812A	TGAAGCCGGCGGCGGCCAGCGTC	GACGCTGGCCGCCGCCGGCTTCA
E821A	CGCCCAGGCACGCGCCGTACTGC	GCAGTACGGCGCGTGCCTGGGCG
D825A	CGGGCGTTGATGGCGCCCAGGCACT	AGTGCCTGGGCGCCATCAACGCCCG
D830A	GCGCAGATCAGGGCGCGGGCGTTGA	TCAACGCCCGCGCCCTGATCTGCGC
E821A/D825A	CGGGCGTTGATGGCGCCCAGGCACG	CGTGCCTGGGCGCCATCAACGCCCG
E821A/D830A	GCGCAGATCAGGGCGCGGGCGTTGA	TCAACGCCCGCGCCCTGATCTGCGC
D825A/D830A	GCGCAGATCAGGGCGCGGGCGTTGA	TCAACGCCCGCGCCCTGATCTGCGC
E821A/D825A/D830A	GCGCAGATCAGGGCGCGGGCGTTGA	TCAACGCCCGCGCCCTGATCTGCGC

SI Table S1. List of primers used to generate SARS-CoV S mutants.